Mon. Not. R. Astron. Soc. **316**, 1–18 (2000)

Extended gas in Seyfert galaxies: near-infrared observations of 15 active nuclei

Cláudia Winge,[1★]†‡ Thaisa Storchi-Bergmann,[1★] Martin J. Ward[2★] and Andrew S. Wilson[3,4★]

[1]*Instituto de Física, UFRGS, Av. Bento Gonçalves, 9500, CP 15051, CEP 91501-970, Porto Alegre, RS, Brazil*
[2]*Department of Physics and Astronomy, University of Leicester, University Road, Leicester LE1 7RH*
[3]*Astronomy Program, University of Maryland, College Park, MD 20742, USA*
[4]*Space Telescope Science Institute, 3700 San Martin Drive, Baltimore, MD 21218, USA*

Accepted 2000 January 5. Received 1999 October 21; in original form 1999 August 24

ABSTRACT

Results from an analysis of low-resolution ($R \sim 250$) near-infrared long-slit spectra covering simultaneously the *I*, *J*, *H* and *K* bands, for a sample of 15 Seyfert galaxies and the NGC 5253 starburst nucleus, are presented. The Seyfert galaxies were selected as presenting 'linear' or cone-like high-excitation emission lines in the optical, most probably arising from the collimation of the radiation of the central source by a dusty molecular torus. Our goal was to look for signatures of this torus, and to investigate the gaseous distribution, excitation and reddening. The strongest emission lines detected are usually He I 1.083 μm and [S III] λ9532, followed by Paβ. In some cases, [Fe II] 1.26 and 1.64 μm are also seen. [Fe II] 1.26 μm and H_2 $v = 1 - 0$ S(1) are detected in some of the higher resolution spectra obtained for five galaxies. The emission lines are spatially extended in most cases, and we have used the [Fe II]/Paβ ratio as a measure of the gaseous excitation in Mrk 573, NGC 1386 and NGC 7582. Values for this ratio between 1.5 and 6 are found, suggesting excitation of [Fe II] by X-rays or shock waves in some regions. Broad permitted lines are observed in three Seyfert 1 galaxies. Nuclear Paβ in NGC 1365 and possibly nuclear Brγ in Mrk 573 are also broad.

From analysis of the spatial distribution of the continuum ($J - H$) and ($H - K$) colours derived from our spectra, we find redder colours for the nucleus than for the nearby bulge in most of the Seyfert 2s observed. Comparison with models including emission from dust and stars shows that hot ($T \sim 1000$ K) dust emission dominates the nuclear continuum in NGC 1365, NGC 2110, NGC 3281, NGC 7582 and ESO 362-G18. In NGC 1386, 5643 and 5728 the main contributor is the underlying stellar population, combined with some foreground reddening and/or cooler dust emission. In a few cases, the ($J - H$) colours on opposite sides of the nucleus differ by 0.3–0.8 mag, an effect that we interpret as partly resulting from differences in the local stellar population, and possibly extinction gradients.

Key words: galaxies: active – galaxies: Seyfert – infrared: galaxies.

1 INTRODUCTION

In the unified model for active galactic nuclei (AGN), the nuclear engine is surrounded by an optically thick, dusty toroidal structure, which collimates the escaping photons and, at the same time, hides the true nucleus from our line of sight (Antonucci 1993). Observational evidence for such a model comes from optical spectropolarimetry, which reveals that a number of Seyferts 2s show broad emission lines and blue continuum in polarized light (Miller & Goodrich 1990; Tran 1995), and emission-line imaging, which shows elongated morphologies for the extended emission-line regions, with striking conical or biconical structures which can be traced down to a few tens of parsecs from the nucleus and which are generally aligned with the radio ejecta (Pogge 1989; Storchi-Bergmann & Bonatto 1991; Wilson & Tsvetanov 1994).

There are few observational constraints on the geometry of the torus, although red features and dust lanes (e.g. Wilson et al. 1993;

★ Visiting Astronomer at the Cerro Tololo Interamerican Observatory.
† CNPq Fellowship.
‡ E-mail: winge@if.ufrgs.br

Table 1. Log of observations.

Object	Date	PA (°)	Grating/Band	Exp. Time (sec)	Slit width (arcsec)	Spatial scale (pc/arcsec)
NGC 526A	1995 Oct 30	123	XD	1100	1.1	373
NGC 1097	1995 Oct 31	77	LR J	1200	1.1	82
NGC 1365	1995 Oct 30	130	XD	600	1.1	106
	1995 Oct 31	145	LR J	2400	1.1	
NGC 1386	1996 Feb 28	0	XD	800	1.1	56
NGC 2110	1996 Feb 28	350 (r)	XD	800	1.1	148
NGC 3281	1996 Feb 28	45	XD	800	1.1	224
NGC 4388[a]	1996 Feb 27	13	XD	1200	1.1	78
	1996 Feb 27	90 (p)	XD	800	1.1	
	1996 Feb 29	13	HR J	2200	1.7	
	1996 Feb 29	90 (p)	HR J	2200	1.7	
NGC 5253	1996 Feb 28	43	XD	400	1.1	26
NGC 5643	1996 Feb 28	90	XD	800	1.1	78
NGC 5728	1996 Feb 28	20 (p)	XD	400	1.1	180
	1996 Feb 28	110	XD	800	1.1	
NGC 7582	1995 Oct 30	203	XD	900	1.1	102
IC 5063[b]	1995 Nov 01	90	LR K	2520	1.1	220
ESO 362-G18	1995 Oct 30	68 (p)	XD	900	1.1	245
Fairall 9	1995 Oct 30	123	XD	600	1.1	911
Mrk 509	1995 Oct 30	0	XD	600	1.1	667
Mrk 573	1995 Oct 31	125 (r)	LR J	3000	1.1	335
	1995 Nov 01	35 (p)	LR K	3240	1.1	

[a] Bad seeing (~2.5 arcsec) for the HR spectra at PA = 13°.
[b] Clouds.

Simpson et al. 1996b) aligned perpendicular to the radio/extended line emission axis are seen in some high-resolution images. Hot dust ($T \sim 1200$ K) has been found to be an important contributor to the near-infrared nuclear continuum of Seyfert galaxies (Glass & Moorwood 1985; Kotilainen et al. 1992; Alonso-Herrero et al. 1998, hereafter AH98). Theoretical models (Krolik & Begelman 1988) show that, for the dust to reach this temperature, the inner edges of the torus must be only a few parsecs from the nuclear source. The total extent of the torus, however, is not well constrained, and may reach several tens or even a hundred parsecs. Warm dust ($T \approx 600$–800 K) is presumably responsible for the observed mid-infrared flux (Pier & Krolik 1993).

Infrared spectroscopy of a number of Seyfert 2 galaxies has revealed broad components in the hydrogen emission lines (e.g. Veilleux, Goodrich & Hill 1997, and references therein), thus confirming, at least in those particular cases, the presence of an obscured broad-line region. The torus is expected to contain warm molecular hydrogen, the vibration–rotational transitions of which, especially H_2 $v = 1 - 0$ S(1), could be used as a tracer of the size and geometry of the toroidal structure (Blietz et al. 1994; Moorwood et al. 1996; Marco, Alloin & Beuzit 1997). On the other hand, while the H_2 emission is expected to be extended perpendicular to the collimation/radio emission axis, emission lines from ionized gas (such as [Fe II] 1.26 μm) should be emitted preferentially along the collimation axis, either via photoionization by the hard photons from the central source, or by shocks from the interaction of the radio jet with the ambient gas.

To address these issues, we have obtained long-slit spectra in the near-infrared *I*, *J*, *H* and *K* bands of a sample of Seyfert galaxies with known elongated or biconical high-excitation optical emission, which, in the unified model, is a direct result of the presence of the collimating torus. We have also observed NGC 5253, a classical H II galaxy. Our first results, on NGC 2110 and the Circinus galaxy, have already been published (Storchi-Bergmann et al. 1999, hereafter Paper I), and in this paper we present the data for the remaining galaxies observed.

2 DATA REDUCTION

Long-slit spectra of the sample galaxies were obtained using the Infrared Spectrograph (IRS) on the 4-m 'Blanco' telescope of the Cerro Tololo Interamerican Observatory (CTIO) in 1995 October–November and 1996 February–March 1996. The detector used was a 256 × 256 InSb device, with a 0.363 arcsec per pixel scale. The useful slit length was about 15 arcsec, and the slit width was either 1 or 1.7 arcsec, depending on the seeing, which was generally between these two values. The majority of the spectra were obtained using a low-resolution ($R \sim 250$), cross-dispersed grating (hereafter, the XD grating), which splits the complete 0.9–2.3 μm spectra into four or five segments, roughly coincident with the *R*, *I*, *J*, *H* and *K* spectral bands. A few galaxies were also observed using either a 75 line mm^{-1} grating, with resolution $R \sim 700$ (4 pixels), hereafter the LR grating, or a 210 line mm^{-1} grating, $R \sim 2000$, hereafter the HR grating.

The log of observations is listed in Table 1. We observed most of the galaxies with the slit aligned along the position angle (PA) of the major axis of the inner isophotes in narrow-band ([O III]) images, or along the radio axis (identified by an 'r' in column 3). In a few cases, spectra were also obtained along the perpendicular direction ('p') or, for the Seyfert 1 objects, along arbitrary PAs. For NGC 5253 the slit was positioned along the major axis of the Hα emission structure in the inner ~25 arcsec. Futher details of the individual spectra are given in Section 3. To obtain the linear spatial scales in Table 1, we adopted $H_0 = 75$ km s^{-1} Mpc^{-1}.

Both XD and LR/HR data were reduced using IRAF scripts kindly provided by R. Elston at CTIO (available at the CTIO ftp archive[1]), and followed standard procedures. The reduction of the LR and HR data has already been described in Paper I. The only difference here is that, after bias subtraction, flat-fielding and sky subtraction, removal of the atmospheric absorption features and

[1] http://www.ctio.noao.edu/instruments/ir_instruments/irs/reductions/README. html

Table 2. Cross-dispersed grating wavelength calibrations.

Run	Band	Range (μm)	Pixel (Å)	rms (Å)
1995 Oct 30	I	0.802–1.195	16	2
	J	0.961–1.435	19	7
	H	1.199–1.792	23	10
	K	1.601–2.364	30	32
1996 Feb 27	I	0.865–1.260	16	3
	J	1.038–1.513	19	3
	H	1.296–1.890	24	7
	K	1.602–2.691	43	66
1996 Feb 28	R	0.772–0.999	13	26
	I	0.851–1.226	16	2
	J	0.972–1.447	19	5
	H	1.213–1.806	24	4
	K	1.616–2.404	31	16

flux calibration were performed on the full frame, instead of on the extracted spectra.

For the XD data, the fundamental difference from the standard infrared data reduction is the tracing of the distortion across the slit (the wavelength direction). This was done using the spectrum of a bright star or pinhole, which was traced in each 'band' with a fourth-order Legendre polynomial in the APTRACE task. Similarly, the flat-fields were created using APNORMALIZE rather than RESPONSE, and then the individual segments of each image (corresponding approximately to the five colour bands) were flat-fielded, and 'straightened' using the solution previously found with the tracing star/pinhole spectrum. Wavelength calibration was performed using an HeAr lamp, with different solutions for each 'band'. Low (2–4) order Legendre polynomials were fitted to a sample of four (K) to 12 (R) lines, resulting in the spectral intervals, pixel scales and rms residuals of the fits listed in Table 2. Atmospheric absorption correction and flux calibration followed the same procedures as for the LR/HR data.

3 RESULTS

The integrated spectra of the sample galaxies, corresponding to the co-added emission within a 7–8 arcsec spatial window, are shown in Figs 1(a)–(e) for the XD data. For the LR/HR data, the extraction windows were as listed in Table 4 (see later), and the resulting integrated spectra are shown in Figs 2(a) and (b). Inside the atmospheric absorption bands, the XD data were masked out when the signal was below 10 per cent of the peak transmission in the uncalibrated frames. The main emission lines are indicated, and total line fluxes are listed in Tables 3 and 4. In the XD sub-sample, the strongest lines are the He I + Paγ blend and [S III] λ9532 emission. The uncertainties in the integrated fluxes are dominated by the continuum placement, and we estimate them to be of the order of 20–25 per cent for the XD spectra, and 10–20 per cent for the LR/HR data.

Table 5 lists the full width at half-maximum (FWHM), corrected for instrumental resolution, of the lines observed at different positions for the four objects with HR/LR spectra. The errors are due to the uncertainty in the placement of the continuum and represent maximum values. Owing to its higher signal-to-noise (S/N) ratio, the emission lines in a spectrum of the planetary nebula NGC 7009 were used as the reference (instrumental) profile for the LR grating. These values were found to be in very good agreement with the FWHM of the sky lines. For the HR grating the instrumental profile was given by the HeAr calibration lamp lines.

3.1 Extended emission and line ratios

Owing to the low spectral resolution of the XD spectra, we opted to extract the emission-line spatial distributions directly from the two-dimensional frames, rather than extracting a number of spectra along the slit and measuring the individual line fluxes as done in Paper I. The spatial profiles were obtained by extracting and co-adding all columns inside a spectral window wide enough to contain all the line emission, and the underlying continuum subtracted by linear interpolation between two windows at each side of the emission line. The errors were estimated by creating an image with the same ratio of the rms to the total raw counts ($\sqrt{N}/N$) in each pixel on the uncalibrated frames, then processing those images with the same procedure as used for the actual data.

With the exception of NGC 5253, where the geometric centre of the slit was arbitrarily set as the origin of the spatial axis, the centroid of a nearby continuum spatial profile was used as the origin of the emission-line spatial distributions. No correction for foreground (Galactic) reddening was applied.

In most XD spectra, the emission lines with enough S/N ratio to allow the construction of meaningful spatial profiles were [S III] λ9532, the He I + Paγ blend and Paβ. The available emission lines allowed the determination of the internal reddening only in the H II galaxy NGC 5253, where we found average reddening-corrected values of 3.1 and 4.7 for the (He I + Paγ)/Paβ and [S III] λ9532/Paβ ratios, respectively. For the other galaxies, a good determination of the narrow-emission-line reddening could not be obtained, and any comparison among the resulting line ratios should be considered with caution. Some regularity was observed between the Seyfert 1 galaxies, which presented integrated line ratios (He I + Paγ)/Pa$\beta \approx 3.4$ and [S III] λ9532/ Pa$\beta \approx 0.4$. For the Seyfert 2 nuclei, these same ratios span the ranges $1.0 \lesssim$ (He I + Paγ)/Pa$\beta \lesssim 4.9$ and $0.6 \lesssim$ [S III] λ9532/ Pa$\beta \lesssim 6.7$.

We now describe the spatial distribution of the emission lines for each galaxy, comparing the light profiles in the emission lines with that of a reference star, and also the spatial variations in the available line ratios. For reasons of clarity in the figures, the emission-line spatial profiles shown below have been rebinned to 0.74 arcsec per pixel.

NGC 5253. The spectrum of this H II galaxy (Fig. 1a, top panel) was obtained along the PA of the major axis of the Hα emission structure seen in fig. 1(a) of Calzetti et al. (1997), with essentially no stellar continuum detected. The strong emission lines (Fig. 3) extend over ~10 arcsec and peak at the central clump, corresponding to the starburst nucleus. To investigate their variation with distance from the nucleus, we constructed several line ratios. The [S III] λ9532/(He I + Paγ) ratio varies from ~1.2 at 3 arcsec south-west to ~2.8 at 3 arcsec north-east, while the [S III] λ9532/Paβ ratio is almost flat in the above interval, 2.78 ± 0.96, rising slightly to the south-west. The average reddening in the region $-3 < r < 4.5$ arcsec, calculated from the Brγ/Paβ ratio, assuming a case B intrinsic value of 0.171 (Osterbrock 1989), is $E(B-V) \sim 0.91 \pm 0.15$. However, large variations [as much as ~3 mag in $E(B-V)$] are found within a few pixels, in agreement with the work of Calzetti et al. (1997), which detected a much higher reddening inside the emission clumps than indicated by the emission-line ratios in the integrated optical spectrum. The (He I + Paγ)/Paβ ratio, which can be interpreted as a tracer of the ionization structure, varies from ~2 in the extended regions to up to 5.4 in the starburst nucleus. Assuming a case B recombination, and $A_V = 3$–6 mag, the contribution of Paγ to the blend varies between 0.45 and 0.36 of the Paβ flux. For the above range of

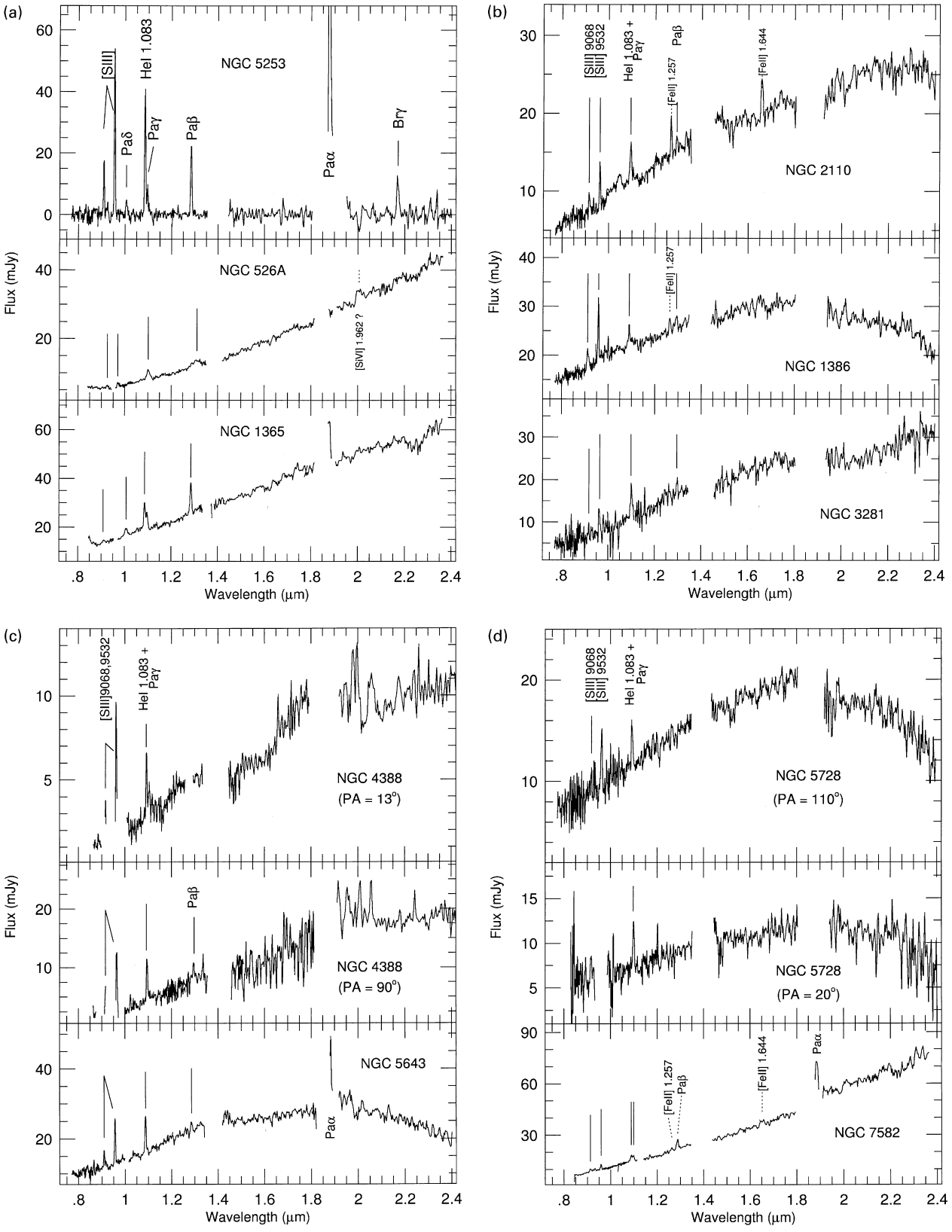

Figure 1. Integrated spectra of the galaxies observed with the XD grating. (a) NGC 5253, 526A and 1365; (b) NGC 2110, 1386 and 3281; (c) NGC 4388 (PA = 13° and 90°) and NGC 5643; (d) NGC 5728 (PA = 110° and 20°) and NGC 7582; (e) ESO 362-G18, Mrk 509 and Fairall 9.

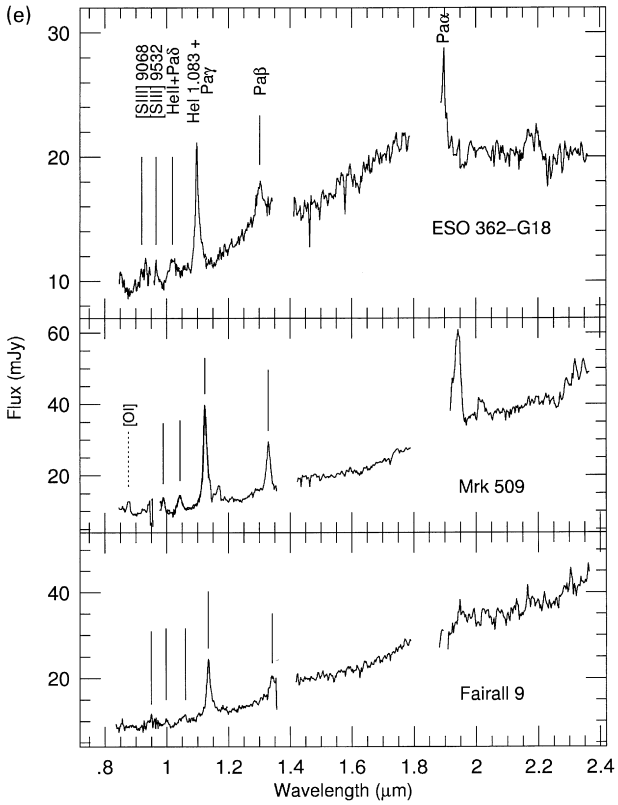

Figure 1 – *continued*

reddening, the observed line ratios translate to $2.6 \lesssim$ He I 1.083 μm/Pa$\beta \lesssim 3.5$, $1.9 \lesssim$ [S III] λ9532/He I 1.083 μm $\lesssim 2.2$ (both ratios corrected for the Paγ contribution) and $4.7 \lesssim$ [S III] λ9532/Pa$\beta \lesssim 7.8$. The upper limits are consistent with H II region models (Lumsden & Puxley 1996).

NGC 526A. The XD spectrum (Fig. 1a, middle) was obtained along the PA of the major axis of the [O III] emission (Mulchaey, Wilson & Tsvetanov 1996), and presents a steep continuum with faint emission lines. We detected the He I + Paγ blend, Paβ, and a feature at ~1.96 μm which we tentatively identify as [Si VI] 1.962 μm. The lines are only barely spatially resolved (Fig. 4), with Paβ presenting some low surface brightness emission up to ~4 arcsec south-east. The (He I + Paγ)/Paβ ratio in the inner 4 arcsec ($|r| < 2$ arcsec) is 1.31 ± 0.13.

NGC 1365. The XD spectrum (Fig. 1a, bottom), obtained along the axis of the ionization cone at PA = 130°, shows a red continuum, with prominent permitted lines (He II + Paδ, He I + Paγ, Paβ); Paα is detected above the atmospheric absorption. The emission (Fig. 4) is resolved and similarly extended symmetrically from the nucleus in all lines, with the exception of a feature in He I + Paγ at ~4 arcsec north-west (the 'anti-cone' direction) which can be associated with an optical hotspot in the circum-nuclear star-forming ring (Storchi-Bergmann & Bonatto 1991; Kristen et al. 1997).The line ratios (He I + Paγ)/Paβ and (He II + Paδ)/(He I + Paγ) are essentially constant in the inner 4 arcsec, with values of 2.27 ± 0.12 and 0.19 ± 0.02, respectively.

This galaxy was also observed with the LR grating in the *J* band. The spectrum (Fig. 2a, middle) shows very clearly the presence of a broad component in the nuclear Paβ profile (Fig. 5). The FWHM of the nuclear and extranuclear profiles, obtained

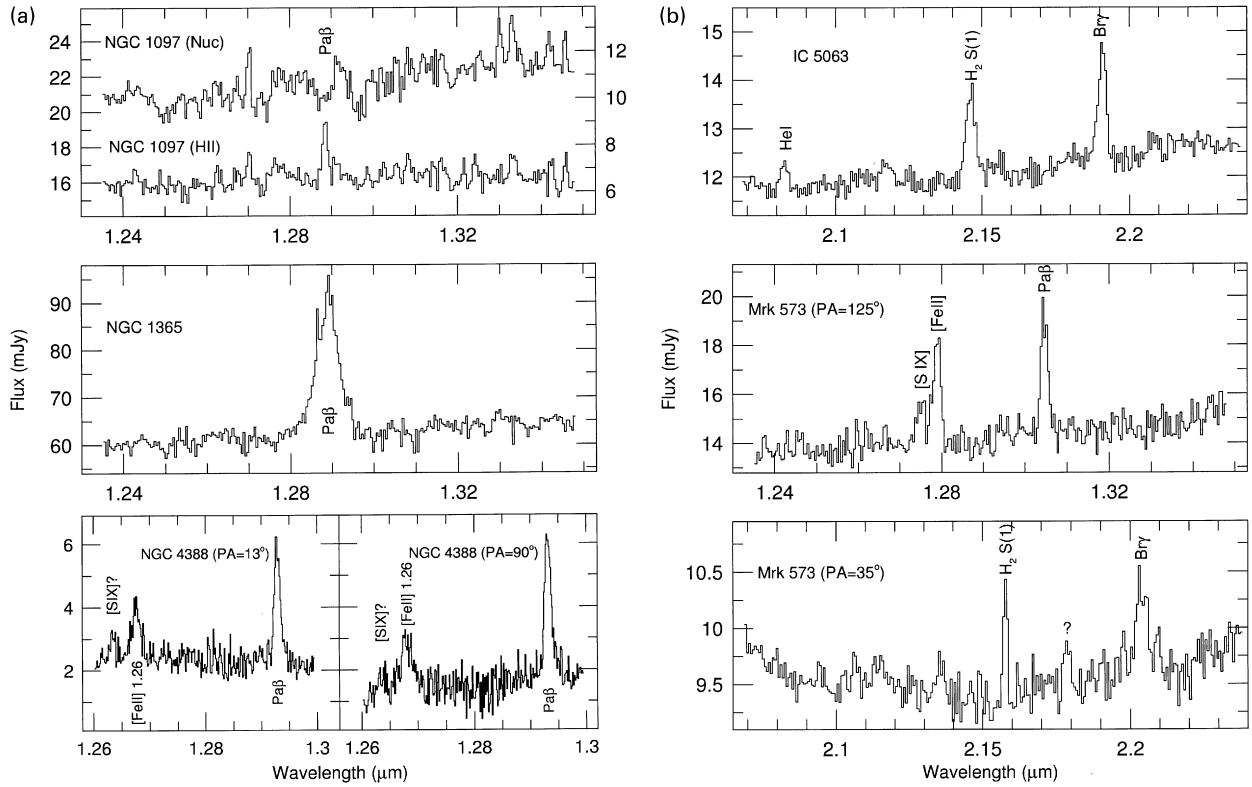

Figure 2. Integrated spectra of the sample galaxies observed with the LR/HR gratings. (a) NGC 1097 – LR/*J*, NGC 1365 – LR/*J*, NGC 4388 – HR/*J* (PA = 13° and 90°). The right-hand scale in the top panel is the flux scale for the H II region spectrum in NGC 1097. (b) IC 5063 – LR/*K*, Mrk 573 – LR/*J* (PA = 125°) and Mrk 573 – LR/*K* (PA = 35°).

Table 3. Integrated line fluxes from the spectra obtained with the XD grating (in units of 10^{-14} erg cm^{-2} s^{-1}).

Object	Line ID	Flux
NGC 526A	[S III] 9532	3.9
	He I + Paγ	11.7
	Paβ	11.5
NGC 1365	[S III] 9532	11.5
	Paδ	3.1
	He I 1.083	26.6
	Paγ	14.7
	Paβ	20.2
NGC 1386	[S III] 9068	6.5
	[S III] 9532	16.1
	He I + Paγ	6.6
	[Fe II] 1.26	5.3
	Paβ	3.5
NGC 2110	[S III] 9068	4.9
	[S III] 9532	11.8
	He I + Paγ	10.1
	[Fe II] 1.26	7.0
	Paβ	3.4
	[Fe II] 1.64	6.2
NGC 3281	[S III] 9068	7.6
	[S III] 9532	24.1
	He I + Paγ	7.9
NGC 4388	[S III] 9532	8.4
(PA = 13)	He I + Paγ	5.7
NGC 4388	[S III] 9532	23.1
(PA = 90)	He I + Paγ	11.8
	Paβ	5.6
NGC 5253	[S III] 9068	33.6
	[S III] 9532	94.3
	Paδ	8.7
	He I 1.083	64.8
	Paγ	13.2
	Paβ	31.1
	Paα	121.7
	Brγ	9.1
NGC 5643	[S III] 9068	8.7
	[S III] 9532	23.3
	He I + Paγ	17.3
	Paβ	3.5
NGC 5728	[S III] 9532	14.4
(PA = 110)	He I + Paγ	9.2
NGC 5728	[S III] 9532	11.9
(PA = 20)	He I + Paγ	10.2
NGC 7582	[S III] 9532	5.7
	He I + Paγ	14.7
	[Fe II] 1.26	2.1
	Paβ	7.8
	[Fe II] 1.64	5.0
ESO 362-G18	He I + Paγ	35.0
	Paβ	10.1
	Paα	>10.7
Fairall 9	[S III] 9532	9.0
	He II + Paδ	7.7
	He I + Paγ	51.5
	Paβ	15.3
	Paα	>18.1
Mrk 509	[S III] 9532	13.3
	He II + Paδ	21.9
	He I + Paγ	108.0
	Paβ	33.0
	Paα	>59.1

using multiple Gaussian component decomposition, is listed in Table 5 for this and the other galaxies observed with the LR and HR gratings. At 4 arcsec north-west and south-east, Paβ is barely resolved spectrally (see Table 5).

The nuclear Paβ profile can be described as the sum of narrow

Table 4. Integrated line fluxes from the spectra taken with the LR/HR gratings (in units of 10^{-14} erg cm^{-2} s^{-1})

Object	Window (arcsec)	Line ID	Flux
NGC 1365	10.96	Paβ (broad)	20.8
		Paβ (total)	41.3
NGC 4388	3.65	[S IX]	2.2
(PA = 13)		[Fe II] 1.26	6.7
		Paβ	10.0
NGC 4388	4.38	[Fe II] 1.26	8.9
(PA = 90)		Paβ	12.2
IC 5063	5.12	H_2 S(1)	0.55
		Brγ	0.45
Mrk 573	8.05	[S IX]	0.89
(PA = 125)		[Fe II] 1.26	1.89
		Paβ	2.03
Mrk 573	5.12	H_2 S(1)	0.14
(PA = 35)		Brγ	0.37

The two entries for Paβ in NGC 1365 correspond to the fluxes in the broad component only (FWHM $\approx$ 1500 km s^{-1}; see Table 5) and in all the emission line, respectively.

Table 5. Intrinsic linewidths (km s^{-1}). The upper block are measurements with the LR grating, the lower those with the HR grating.

Object	Position(arcsec)	Line	FWHM
NGC 1365	Nuc	Paβ (N)	<450
		Paβ (B)	1397^{+30}_{-15}
		Paβ (VB)	2868^{+349}_{-729}
	4.02 NW	Paβ	159^{+48}_{-52}
	4.02 SE	Paβ	210^{+53}_{-69}
IC 5063	Nuc	Brγ	<400
		H_2 S(1)	<400
	1.46 NW	Brγ	<400
		H_2 (S1)	483^{+82}_{-73}
Mrk 573 J	Nuc	[S IX]	<450
		[Fe II] 1.26 μm	323^{+54}_{-46}
		Paβ	<450
Mrk 573 J	1.46 NW	[Fe II] 1.26 μm	<450
		Paβ	182^{+127}_{-102}
	1.46 SE	[Fe II] 1.26 μm	<450
		Paβ	323^{+43}_{-127}
	3.29 NW	Paβ	<450
	3.29 SE	Paβ	<450
Mrk 573 K	Nuc	Brγ	589^{+256}_{-135}
		H_2 S(1)	<400
NGC 7009	(instrumental, LR)	Paβ	455^{+8}_{-13}
		Brγ	403^{+10}_{-8}
NGC 4388	Nuc	[Fe II] 1.26 μm	297^{+32}_{-30}
(PA = 13)		Paβ	299^{+69}_{-24}
NGC 4388	Nuc	Paβ	378^{+62}_{-40}
(PA = 90)	1.46 W	Paβ	171^{+48}_{-25}
HeAr	(instrumental, HR)		148 $\pm$ 1

(N), broad (B) and very broad (VB) Gaussian components, with FWHM from 400 to 2900 km s^{-1}. Véron et al. (1980) measured a flux of 7.7×10^{-14} erg cm^{-2} s^{-1} in their broad (FWHM $\sim$ 1300 km s^{-1}) component of Hα. Associating this emission system with the FWHM $\sim$ 1500 km s^{-1} component of Paβ observed here, we obtain a broad line region reddening of $A_V \sim 7.7$ mag for an intrinsic Paβ/Hα ratio of 0.053. Since the broad lines of this galaxy are known to be variable (Giannuzzo & Stirpe 1996), not to mention calibration differences, this value is to be regarded as only a first-order approximation to the actual broad line region reddening.

Recently, Stevens, Forbes & Norris (1999) suggested that the

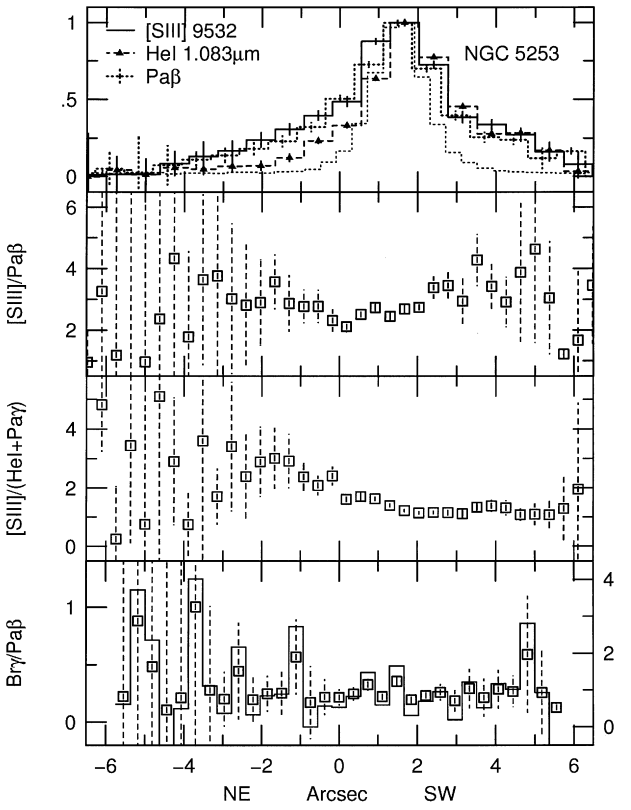

Figure 3. Normalized spatial distributions and line ratios of the main emission lines from the XD spectrum of NGC 5253. The dotted line in the upper panel is the spatial profile of the atmospheric standard star used in the data reduction, and approximately represents the seeing profile. The full line in the bottom panel represents the value of $E(B-V)$ (right axis scale) calculated from the Brγ/Paβ ratio (squares, left axis scale).

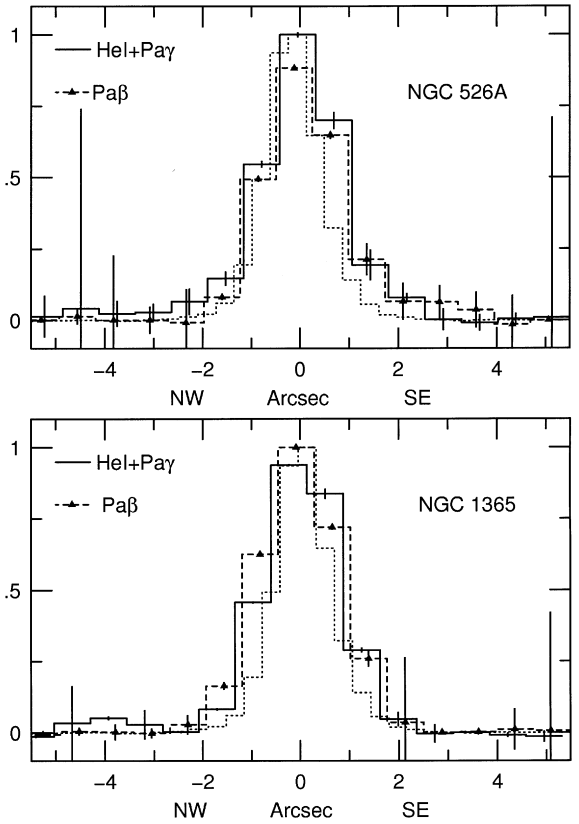

Figure 4. Spatial profiles of the main emission lines from the XD spectrum of NGC 526A (top) and NGC 1365 (bottom). As for NGC 5253, the dotted line is the stellar profile.

optical broad lines in the nucleus of NGC 1365 could originate not at the Seyfert nucleus, but at one of the circumnuclear radio 'hotspots' (Morganti et al. 1999), located at ~5 arcsec south-west of the optical nucleus, as a result of a radio supernova located there. However, we find this highly unlikely, since our spectrum, which was obtained with a 1-arcsec slit, centred in the optical nucleus and oriented at almost right angles to the PA of the hotspot in question, would not have included any of its emission.

NGC 1386. The XD spectrum (Fig. 1b, middle) was obtained along the direction of the high-excitation optical emission-line protrusion detected in the images of Storchi-Bergmann et al. (1996). The brightest line is [S III] λ9532, with fainter He I + Paγ, [Fe II] 1.26 μm, and Paβ. Although noisy, the resulting spatial profiles are definitely extended along the [O III] emission direction (Fig. 6). The He I + Paγ distribution is the most extended, reaching at least 4.5 arcsec north of the nucleus, the end of the slit. The (He I + Paγ)/Paβ ratio is 2.9 ± 1.0 in the inner 4 arcsec. The [S III] λ9532 and [Fe II] 1.26-μm spatial profiles are resolved but more concentrated, extending only up to 2.5 arcsec. In the inner 4 arcsec, the [S III] λ9532/(He I + Paγ) ratio is essentially flat, with a value of 2.21 ± 0.21, while [Fe II] 1.26 μm/Paβ increases from ~0.9 at $r = 2$ arcsec south to ~6 at 2 arcsec north, with a value of ≈2 in the nucleus, indicating a higher excitation of the gas to the north, in agreement with the optical images.

Several mechanisms for the origin of [Fe II] emission in Seyferts have been extensively discussed in previous works

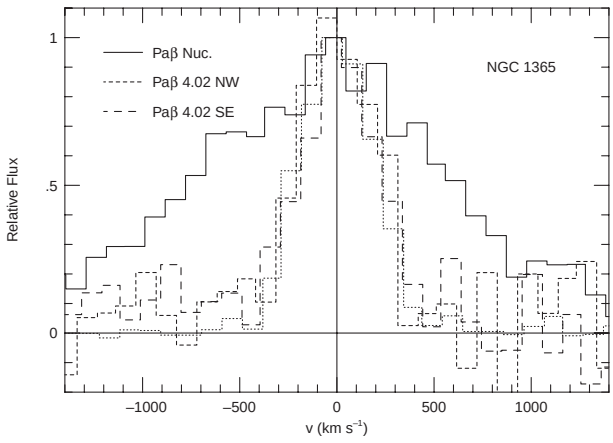

Figure 5. Comparison of the LR Paβ spectral profiles of NGC 1365: nucleus (full line), 4.02 arcsec north-west (short dash), and 4.02 arcsec south-east (long dash). The dotted line is the Paβ profile of NGC 7009, which is taken as representative of the instrumental resolution.

(Forbes & Ward 1993; Simpson et al. 1996a; Alonso-Herrero et al. 1997; Veilleux et al. 1997). In starbursts, if the mechanism generating the [Fe II] emission is directly related to the one producing the radio emission in (radio) bright supernova remnants, Colina (1993) calculated that [Fe II] 1.26/Pa$\beta \leq 0.4$ is expected. The higher ratios observed in Seyferts would then indicate ionization by X-rays from the active nuclei, or by shocks induced by the interaction of an outflow with the surrounding

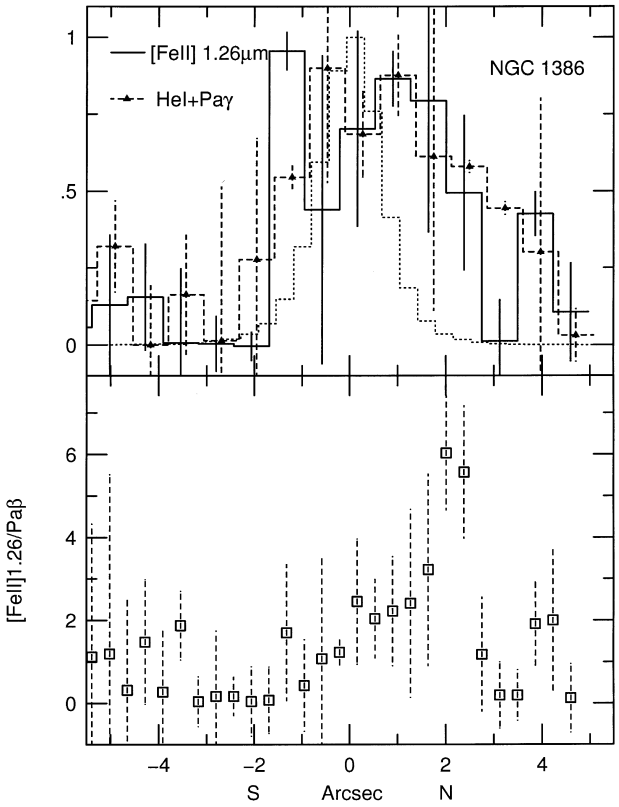

Figure 6. Spatial profiles and [Fe II] 1.26 μm/Paβ line ratio from the XD spectrum of NGC 1386. The dotted line is the stellar profile.

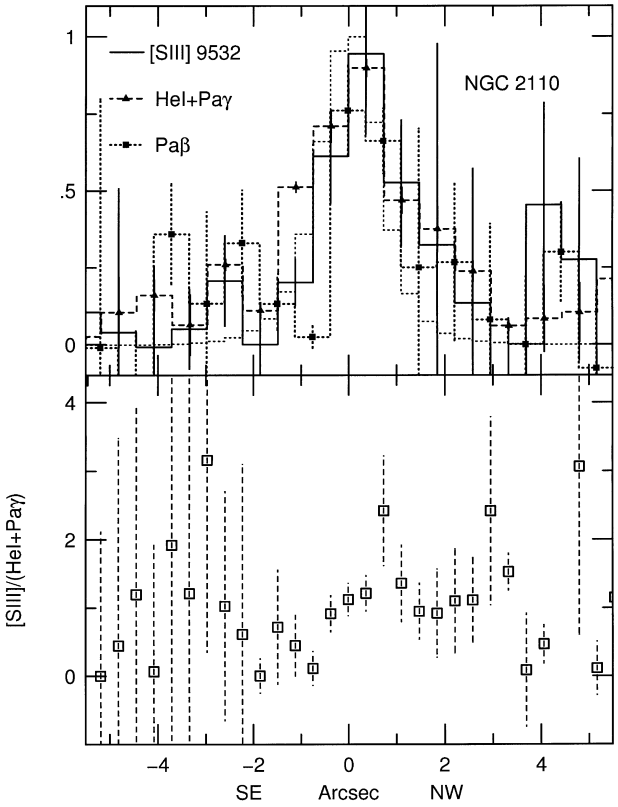

Figure 7. Spatial profiles and [S III] λ9532/He I + Paγ line ratio from the XD spectrum of NGC 2110. The error bars in the [S III] λ9532 profile have been excluded for clarity and are of similar amplitude to those in Paβ. The dotted line is the stellar profile.

medium. However, if the lifetime of the [Fe II] emission phase in single or multiple star formation bursts is longer than in Colina's models, the [Fe II]/Paβ ratio can reach higher values (Vanzi, Alonso-Herrero & Rieke 1998), as the contribution from the remnants becomes dominant over the gas ionization from the ageing H II regions.

Detailed stellar population analysis of NGC 1386 (Schmitt, Storchi-Bergmann & Cid Fernandes 1999) does not indicate the presence of a significant contribution from a young (10 Myr or less) component in the inner 2×2 arcsec^2, and therefore the [Fe II]/Paβ values indicate that, as is also found in NGC 2110 (Paper I), a starburst-related component of the [Fe II] emission is not important in this case. Since this object was not observed with the higher resolution gratings, we do not have any information on the [Fe II] line profile, but the line broadening in Hα and [N II] λ6584 within 1.5 arcsec north of the nucleus detected by Weaver, Wilson & Baldwin (1991) raises the possibility of shocks as an ionization source for the infrared [Fe II] lines. Nagar et al. (1999) find the nuclear radio source to be extended by 0.4 arcsec in PA = 170°, a similar direction to the extension of the optical emission lines.

NGC 2110. The HR/LR data for this galaxy were presented and analysed in Paper I, and we found evidence of shocks and X-rays as dominant sources of excitation for the [Fe II] and H_2 emission in the inner few arcsec, respectively. The XD spectrum shown in Fig. 1(b) (top panel) was obtained along the PA of the radio axis, with [S III] λ9068, [S III] λ9532, He I + Paγ, [Fe II] 1.26 μm, Paβ and [Fe II] 1.64 μm detected. The spatial profiles of [S III] λ9532, He I + Paγ and Paβ are clearly asymmetric (Fig. 7), being extended up to 3 arcsec towards the north-west, the direction of the high-excitation optical emission. The [S III] and Paβ spatial profiles decline more quickly to the south-east than the He I + Paγ profile, consistent with the isophotes in the Hα + [N II] image of Mulchaey et al. (1996). The [Fe II] spatial distribution (already discussed in Paper I) is similar to that of [S III] λ9532. The [S III] λ9532/(He I + Paγ) line ratio rises from 0.44 at 2 arcsec south-east to 1.0 at 2 arcsec north-west. A similar excitation gradient is seen in the [O III] λ5007/Hβ ratio (Wilson, Baldwin & Ulvestad 1985). The H_2 emission, clearly seen in the higher resolution spectra of Paper I, was not detected here because of the low resolution of the XD spectra.

NGC 3281. The XD spectrum is shown in Fig. 1(b) (bottom panel). It shows only faint [S III], He I and Paβ emission. The resulting spatial profiles were of too low a S/N ratio to allow any useful analysis of the extended emission.

NGC 4388. Two sets of data were obtained for this object. The XD spectra (Fig. 1c, top and middle panels) were taken approximately along and perpendicular to the axis of the optical ionization cone, at PA = 13° and 90°, respectively. The S/N ratio is low, with only [S III] λ9532 and He I + Paγ detected. The spatial profiles at PA = 13° (Fig. 8) are noisy, but more extended towards the north-east, the anti-cone direction. The narrow-band Hα + [N II] optical images of Veilleux et al. (1999) show an elongated structure in the inner 10 arcsec, which also appears to be more extended to the north-east (while the cone-like, kpc-scale high-excitation gas distribution is oriented towards the south). Along PA = 90° our emission-line distributions are also resolved, but essentially symmetric with respect to the centre. The line ratios are almost constant in the inner 4 arcsec, with [S III] λ9532/(He I + Paγ) = 1.58 ± 0.84 (PA = 13°) and 1.23 ± 0.74 (PA = 90°). In

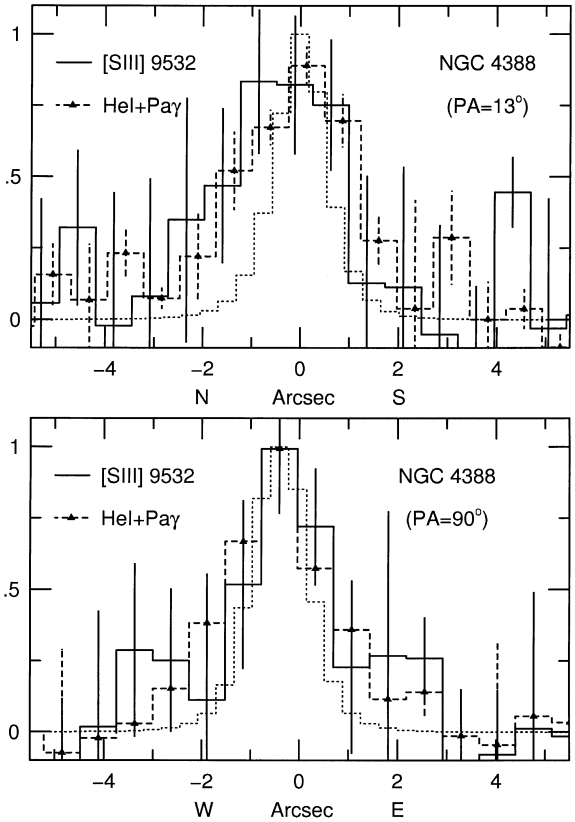

Figure 8. [S III] λ9532 and He I + Paγ spatial profiles from the XD spectra of NGC 4388, at PA = 13° (top) and PA = 90° (bottom).

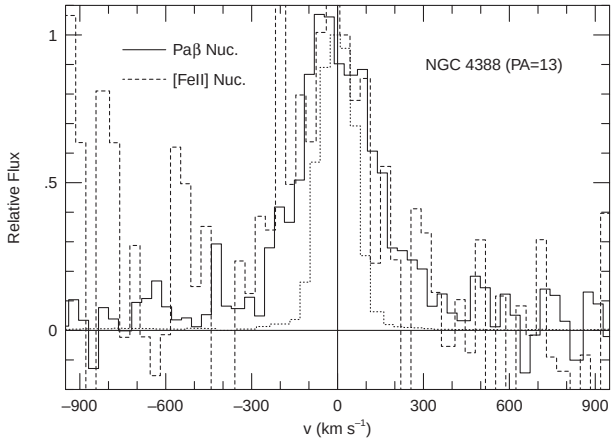

Figure 9. Comparison of the HR Paβ (full line) and [Fe II] 1.26 μm (dashed line) nuclear spectral profiles of NGC 4388 along PA = 13°. The dotted line is the instrumental profile, from the HeAr comparison lamp spectrum.

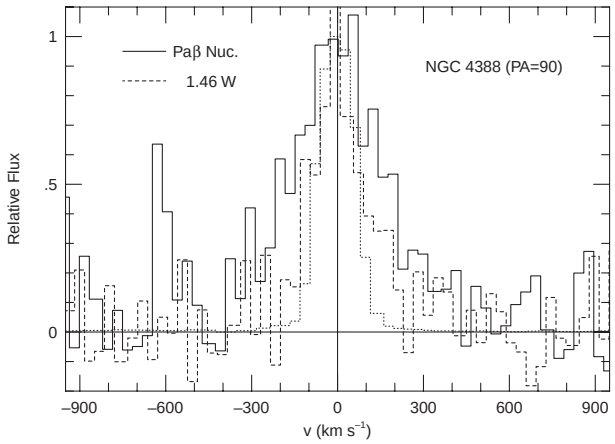

Figure 10. Comparison of the HR Paβ spectral profiles of NGC 4388 along PA = 90° : nucleus (full line) and 1.46 arcsec west (dashed line). The dotted line is the instrumental profile, from the HeAr comparison lamp spectrum.

this latter spectrum, we also measured [S III] λ9532/Paβ $\sim$ 4.30 $\pm$ 0.50 for this same region.

Two HR spectra in the *J* band were obtained at the same position angles as above (Fig. 2a, bottom). The emission-line spatial profiles are only marginally resolved at both PAs, with [Fe II] 1.26 μm/Paβ $\sim$ 0.7. Along the cone direction, we clearly detect [S IX] 1.262 μm.

For the PA = 90° spectrum, the IRS imaging mode was used to find the position of the nucleus in the *K* band, which was found to be located $\sim$1 arcsec north of the optical position. The slit was thus centred offset by this amount from the optical nucleus. However, the continuum is a factor of 2 lower than that of the PA = 13° spectrum, and the [S IX] line is not as clearly detected, suggesting that the true *K*-band nucleus was missed. The spatial offset between the optical and infrared nuclei in NGC 4388 has been previously noted by Stone, Wilson & Ward (1988), who found that the 10-μm emission peaks 'several arcsec' north of the optical nucleus, raising the possibility of the mid-infrared source being associated with the radio ejecta, rather than with the nucleus proper.

The nuclear line profiles of Paβ and [Fe II] 1.26 μm from the PA = 13° spectrum are spectrally resolved, and very similar to each other (Fig. 9). Correcting the observed widths in Table 5 by the instrumental broadening (adopted as the FWHM of Paβ in NGC 7009) gives an intrinsic FWHM of $\sim$300 km s^{-1} for both lines. Along the perpendicular direction (PA = 90°), the nuclear Paβ profile is resolved and marginally broader than at PA = 13°, with a corrected FWHM of $\sim$378 km s^{-1}. At 1.5 arcsec west of the nucleus the line is essentially unresolved (Fig. 10).

NGC 5643. The XD spectrum (Fig. 1c, bottom) was obtained along the axis of the optical ionization cone, and shows [S III], He I 1.083 μm, Paβ, and the tip of the Paα emission line. Only the Paβ profile is marginally resolved spatially in the central regions, but both this line and [S III] λ9532 show a second emission feature $\sim$3 arcsec east of the nucleus, which may be associated with the filamentary extended emission seen in optical images (Schmitt, Storchi-Bergmann & Baldwin 1994; Simpson et al. 1997). In the central 2 arcsec, we measured [S III] λ9532/(He I + Paγ), [S III] λ9532/Paβ and (He I + Paγ)/Paβ ratios of 1.34 $\pm$ 0.62, 6.98 $\pm$ 1.03 and 5.18 $\pm$ 0.71, respectively.

NGC 5728. Two spectra (Fig. 1d) were obtained with the XD grating, at PA = 110°, the optical ionization cone direction, and perpendicular to it (PA = 20°). The S/N ratio is low, and only [S III] λ9532 and He I + Paγ are detected. The spatial profiles, shown in Fig. 11, are resolved along both directions, although more extended at PA = 110° as expected from the optical images of Wilson et al. (1993). However, while He I + Paγ is almost symmetric, the [S III] λ9532 emission is stronger to the north-west, the opposite direction to the optical cone. The [S III] λ9532/(He I + Paγ) ratio in the inner 4 arcsec is 2.19 $\pm$ 0.85 along the cone, and 1.63 $\pm$ 0.94 perpendicular to it.

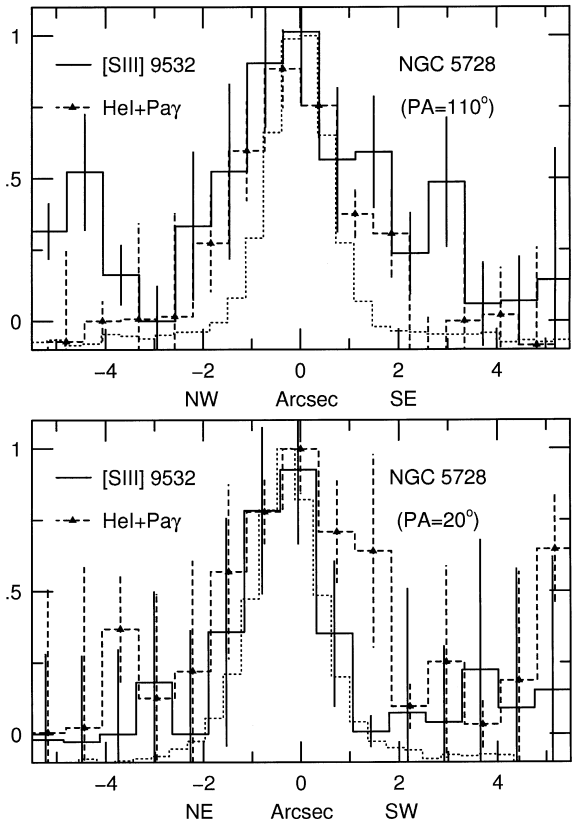

Figure 11. Spatial line profiles from the PA = 110° (top) and PA = 20° (bottom) XD spectra of NGC 5728. The error bars in the He I + Paγ profile have been omitted for clarity and are of similar amplitude to those in the [S III] λ9532 distribution. The dotted line is the stellar profile.

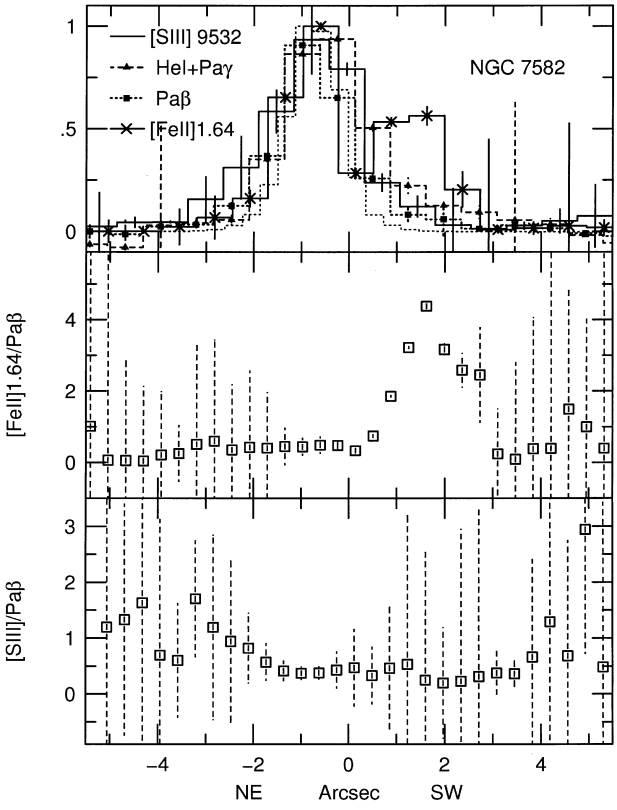

Figure 12. Spatial profiles and line ratios from the XD spectrum of NGC 7582. The dotted line is the stellar profile. Note that the origin of the spatial axis corresponds to the nearby *continuum* peak for each line.

NGC 7582. This galaxy was observed with the slit at PA = 203°, which is within the optical ionization cone which has its axis in PA $\approx$ 250° (Storchi-Bergmann & Bonatto 1991). The peaks of the emission-line spatial profiles (Fig. 12, top panel), are offset from the peak of the nearby continua by 0.7–0.8 arcsec to the north-east, the opposite direction to the ionization cone. All emission lines, with the possible exception of Paβ, are extended towards the cone. The [Fe II] 1.64-μm emission presents a double-peaked structure, with an unresolved core plus a secondary bump reaching $\sim$2.5 arcsec south-west. The [S III] λ9532 profile is marginally extended to the north-east. The double-peaked structure of the [Fe II] 1.64-μm emission is evident in the line ratio distribution: to the north-east, the [Fe II] 1.64 μm/Paβ ratio (Fig. 12, middle) is essentially constant at 0.45 $\pm$ 0.08, reflecting the similar light distribution of the two lines; to the south-west, the ratio increases sharply to 4.4 at 1.6 arcsec, and then falls back to $\sim$0.3 at 2.5 arcsec.

In the absence of significant reddening, and taking the intrinsic ratio between the [Fe II] $\lambda\lambda$ 1.64- and 1.26-μm lines as 0.75, these values translate to a [Fe II] 1.26 μm/Paβ ratio between 0.6 and 6, similar to those found above for NGC 1386 or in Paper I for the extended high-excitation gas in NGC 2110. Note that, contrary to what was observed for NGC 2110, where the nuclear [Fe II]/Paβ ratio was quite high ($\sim$7), the nucleus of NGC 7582 presents a much lower ratio than the extended emission, with only a small excess over the expected ratio for young starbursts. Towards the cone, however, the tenfold increase in the [Fe II]/Paβ ratio suggests the presence of an additional source of ionization, either excitation by X-ray photons from the active nucleus, escaping preferably towards the cone (owing to shadowing by the torus), or the interaction of the radio plasma with the ambient medium. The recent radio maps of Morganti et al. (1999) show that the 3.5-cm emission is indeed extended and spatially coincident with the inner regions of the extended Hα and [O III] emission (Storchi-Bergmann & Bonatto 1991).

If there were significant intervening reddening ($A_V \sim 13$ mag from the [Fe II] 1.64 μm/1.26 μm integrated line ratio from Table 3; or $A_V \lesssim 8$ mag from the continuum colours, see Section 3.2), the above observed values would translate to an intrinsic ratio [Fe II] 1.26 μm/Pa$\beta \gtrsim 1$ in the cone region, still requiring an additional source of ionization other than young starbursts. A corresponding increase towards the south-west is not observed in the [S III] λ9532/Paβ ratio (Fig. 12, bottom), where we measured values of 0.61 $\pm$ 0.29 ($r < 3$ arcsec north-east) and 0.34 $\pm$ 0.13 ($r < 3$ arcsec south-west).

ESO 362-G18. Our XD spectrum of this Seyfert 1 galaxy (Fig. 1e, top) was obtained along PA = 68°, which is perpendicular to the direction of the axis of the approximately cone-shaped high-excitation gas emission region (Mulchaey et al. 1996). The spectrum presents bright broad lines including He II + Paδ, He I + Paγ, Paβ and Paα, which is located close to the atmospheric absorption between the *H* and *K* bands so the flux must be regarded as a lower limit. The spatial profiles of the permitted lines (Fig. 13) are extended towards the south-west, which can be identified with the emission structure seen in the optical Hα + [N II] images of Mulchaey et al. (1996). The distribution of the (He I + Paγ)/Paβ line ratio is approximately symmetric, with a maximum of $\sim$7.2 about 0.5 arcsec south-west

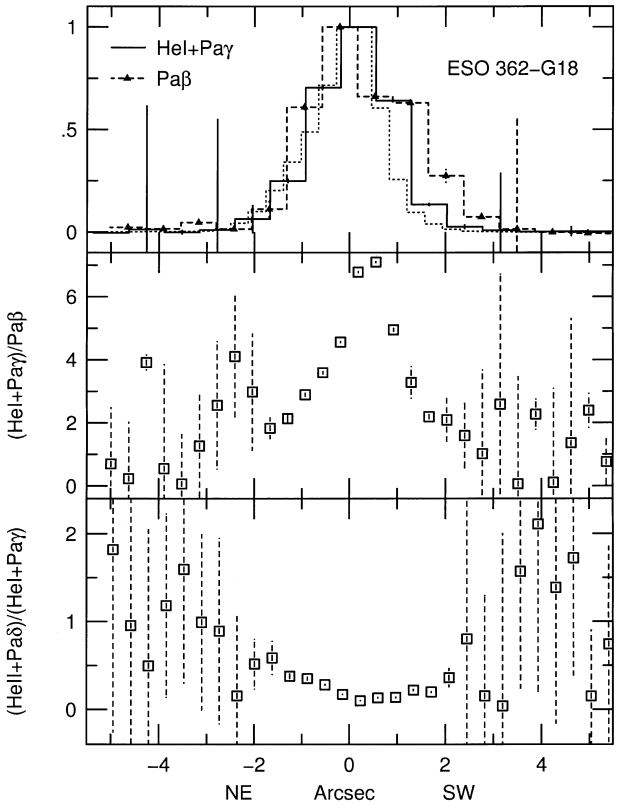

Figure 13. As Fig. 12, for ESO 362-G18.

of the continuum peak, and decreasing to ∼1.5 at 3 arcsec both sides. The behaviour of the (He II + Paδ)/(He I + Paγ) ratio is quite different, with an essentially constant value of 0.29 ± 0.16 in the $r < 2$ arcsec region.

Mrk 509. This is a Seyfert 1 galaxy suggested by Phillips et al. (1983) as presenting a face-on outflow. The XD spectrum in Fig. 1(e, middle) was obtained along the north–south direction. The spatial profiles (Fig. 14, top) are slightly resolved, and more extended towards the south, with the exception of the [S III] λ9532 line, which also shows extended emission up to 3 arcsec north of the nucleus. The line ratios in the inner 4–5 arcsec are dominated by the nuclear source, with [S III] λ9532/Paβ = 0.42 ± 0.13, [S III] λ9532/(He I + Paγ) = 0.10 ± 0.03, (He I + Paγ)/Paβ = 3.50 ± 0.52, and (He II + Paδ)/(He I + Paγ) = 0.19 ± 0.01.

Fairall 9. The XD spectrum of this classical Seyfert 1 nucleus is very similar to that of Mrk 509 (Fig. 1e). The brightest line is also He I + Paγ and the spatial profiles (Fig. 14, bottom) are essentially unresolved, with [S III] λ9532/Paβ, [S III] λ9532/(He I + Paγ), (He I + Paγ)/Paβ and (He II + Paδ)/(He I + Paγ) in the inner 4–5 arcsec of 0.50 ± 0.08, 0.10 ± 0.03, 3.30 ± 0.33 and 0.16 ± 0.01, respectively.

NGC 1097. We obtained an LR spectrum in the *J* band of this LINER nucleus in order to determine if the broad double-peaked profile observed in Hα (Storchi-Bergmann, Baldwin & Wilson 1993) was also present in Paβ. The long-slit spectrum, however, shows Paβ emission only from H II in the circumnuclear star-forming ring, 8.7 arcsec south-west of the nucleus (Fig. 2a, top panel). This is a clear case of a very low-luminosity, rather than dust-obscured, active nucleus.

IC 5063. Only an LR *K*-band spectrum (Fig. 2b, top) was

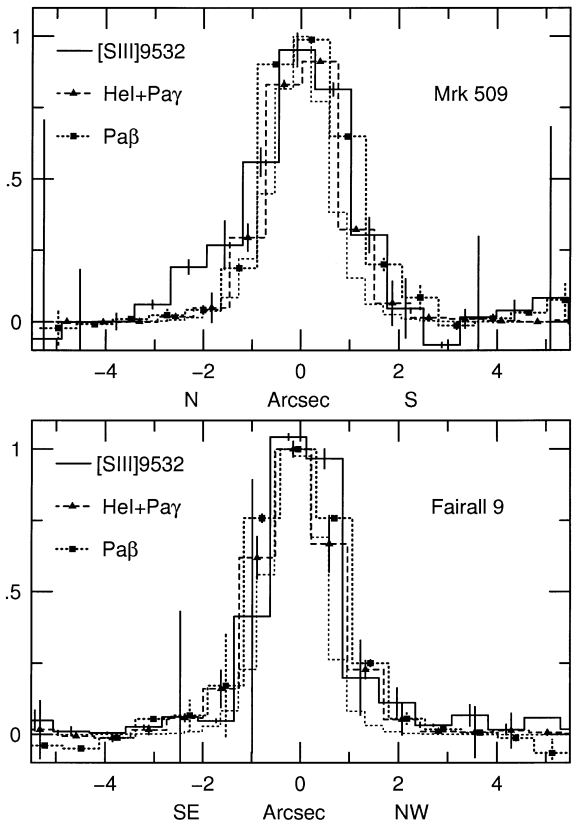

Figure 14. The spatial emission-line profiles from the XD spectra of Mrk 509 (top) and Fairall 9 (bottom). The dotted line is the stellar profile.

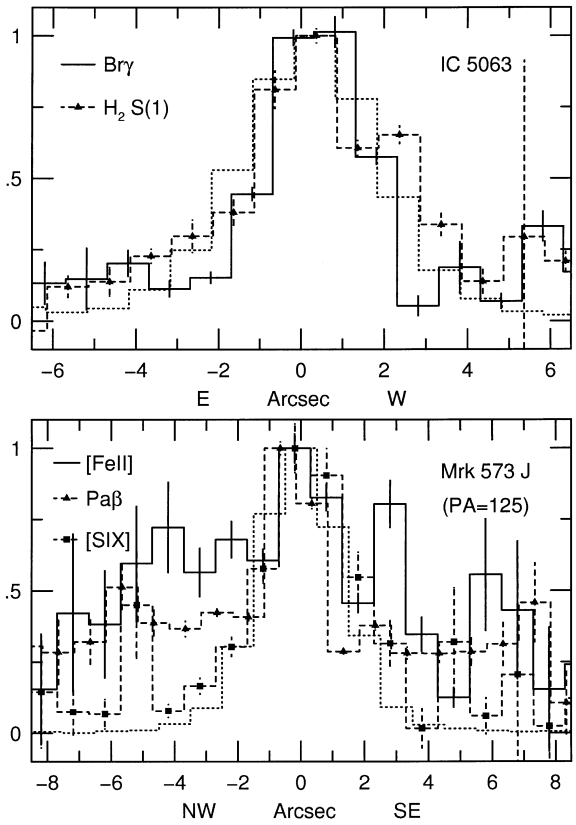

Figure 15. Spatial profiles from the LR spectra of IC 5063 (*K* band, top) and Mrk 573 (*J* band, bottom). The dotted line is a stellar profile.

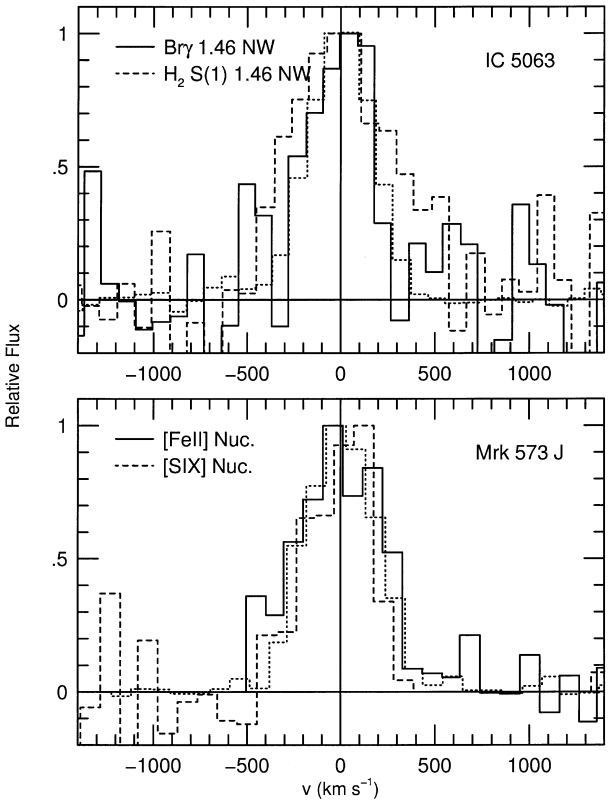

Figure 16. Top: comparison of the LR spectral line profiles of the *K*-band spectrum of IC 5063: 1.46 arcsec north-west Brγ (full line) and H_2 S(1) (dashed line). Bottom: *J*-band (PA = 125°) nuclear spectrum of Mrk 573: [Fe II] 1.26 μm (full line) and [S IX] (dashed line) profiles. The dotted lines in the top and bottom panels are, respectively, the Brγ and Paβ profiles of NGC 7009, which are taken as representative of the instrumental resolution.

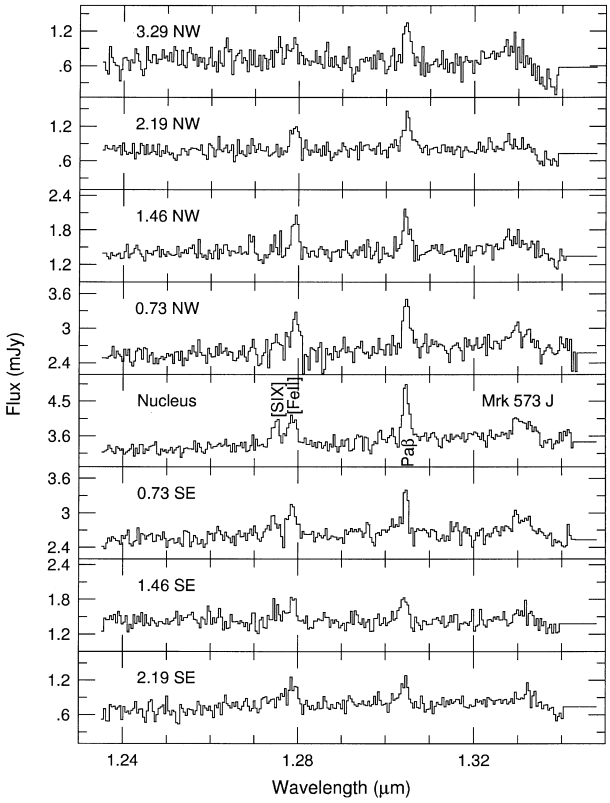

Figure 17. Individual *J*-band spectra for Mrk 573. Bin size is 0.73 arcsec (1.46 arcsec for the outermost position), centred at the distance from the nucleus indicated in the individual panels.

obtained, under non-photometric conditions. The orientation of the slit was PA = 90°, which is close to that of the radio/optical/infrared structures in the inner few arcsec (Simpson, Ward & Kotilainen 1994; Morganti, Oosterloo & Tsvetanov 1998; Kulkarni et al. 1998), and both Brγ and H_2 $v = 1 - 0$ S(1) lines were detected.

The Brγ spatial distribution is unresolved, while the H_2 line appears to be only slightly resolved (Fig. 15, top). The H_2/Brγ ratio can be used to discriminate between the possible excitation mechanisms for H_2 emission: in star-forming regions, where the main heating agent is the UV photons, $H_2/Br\gamma < 1.0$ is expected, while additional H_2 emission excited by shocks or by X-rays from the active nucleus increases the observed values to up to 3 or more in Seyferts (Fischer et al. 1987; Moorwood & Oliva 1990; Kawara, Nishida & Gregory 1990; Veilleux et al. 1997). In our spectrum, we measured $H_2/Br\gamma = 1.22 \pm 0.20$ in the inner 5 arcsec, which constitutes marginal evidence of a contribution from the active nucleus. The luminosity in the H_2 line can be used to estimate the mass of hot molecular hydrogen in the nuclear region. If the hot H_2 molecules are thermalized at $T = 2000$ K, and assuming that the emission in all H_2 lines is 10 times that in the S(1) line (Scoville et al. 1982; Veilleux et al. 1997), the observed H_2 $v = 1 - 0$ S(1) luminosity of $L(H_2) = 1.35 \times 10^{39}$ erg s^{-1} translates into a hot H_2 mass of about 450 $M_\odot$.

The spectral profiles of the H_2 and Brγ lines are unresolved, except for the H_2 emission in the 1.5 arcsec north-west spectrum (Fig. 16, top), which has an observed FWHM of ~630 km s^{-1}, corresponding to a intrinsic width of 484 ± 100 km s^{-1}.

Mrk 573. Two LR spectra were obtained for this galaxy. The *J*-band spectrum (Fig. 2b, middle) was taken along the radio continuum and optical emission-line axis at PA = 125° (Pogge & de Robertis 1995; Falcke, Wilson & Simpson 1998), and presents [S IX], [Fe II] 1.26 μm and Paβ emission. Individual spectra, extracted in 0.73-arcsec increments (Fig. 17), as well as the spatial profiles (Fig. 15, bottom), clearly show that the [S IX] distribution is unresolved, while Paβ and [Fe II] 1.26 μm are extended. The [Fe II] 1.26-μm spatial profile presents a weak central peak with a flat extension towards the north-west, reaching up to ~8 arcsec, while the south-eastern side is less prominent, but equally extended. On the other hand, the Paβ distribution is characterized by a well-defined, spatially unresolved central core, and extended emission of almost equal intensity on both sides of the nucleus. The [Fe II] 1.26 μm/Paβ ratio has a mean value of 0.77 ± 0.14 in the inner 5 arcsec.

A *K*-band LR spectrum of Mrk 573 (Fig. 2b, bottom) was obtained at PA = 35°, perpendicular to the direction of the radio jet. Brγ, possibly broad, and narrow H_2 $v = 1 - 0$ S(1) were detected. Extracted spectra, in increments of 0.73 arcsec, are shown in Fig. 18.

In the *J*-band spectra, along PA = 125°, the spectral profile of Paβ is unresolved up to 3.3 arcsec north-west and south-east. The [S IX] line, detected only in the nuclear spectrum, is also unresolved, while [Fe II] 1.26 μm is marginally resolved spectrally in the nucleus but not outside (Fig. 16, bottom panel). In the *K* band, the H_2 nuclear spectral profile is too noisy to yield any information, while Brγ is clearly resolved (Fig. 19) with an

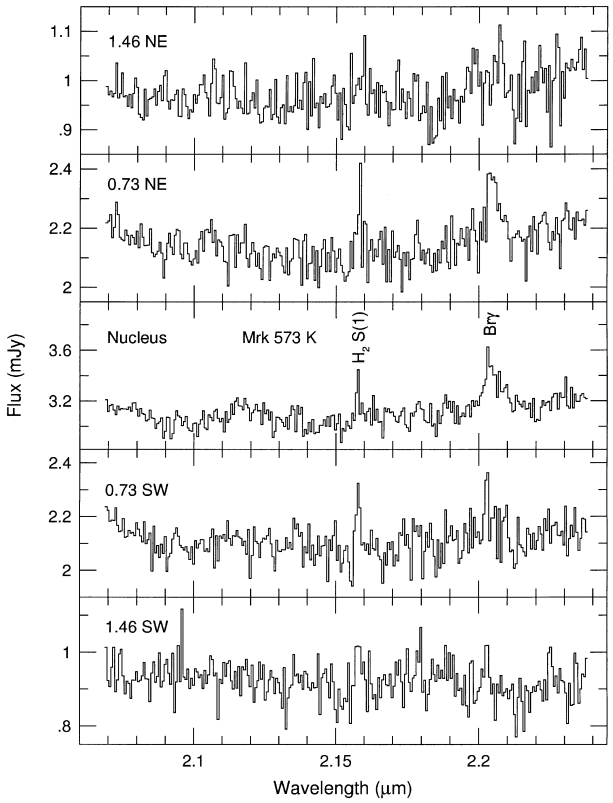

Figure 18. As Fig. 17, for the LR *K*-band spectrum of Mrk 573.

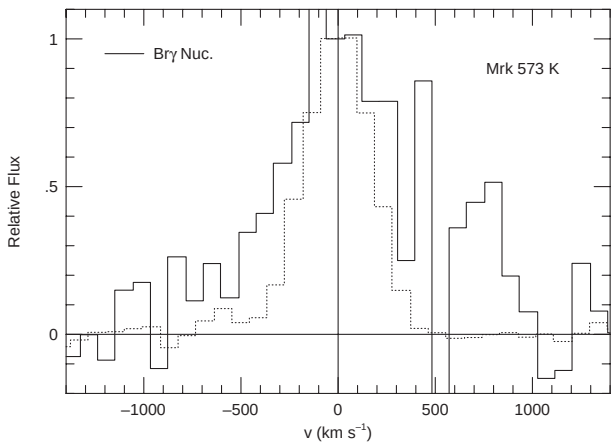

Figure 19. The nuclear Brγ LR spectral line profiles of Mrk 573 (*K* band, PA = 35°). The dotted line is the Brγ profile of NGC 7009, which is taken as representative of the instrumental resolution.

intrinsic width of $\sim$590 km s^{-1}, and some suggestion of a broad component (FWZI $\approx$ 1900 km s^{-1}) which contains about 70 per cent of the total flux in the line, and is not observed in Paβ (FWZI $\lesssim$ 1100 km s^{-1}). Taking the upper limit for the flux of a similar broad component in Paβ as $\sim 5\times10^{-15}$ erg cm^{-2} s^{-1} (calculated from the rms of the continuum around Paβ, and a FWHM of 1300 km s^{-1} obtained from Gaussian decomposition of the Brγ profile), we have Brγ/Pa$\beta \gtrsim 0.6$, implying a reddening of $A_V \gtrsim 9$ mag in our line of sight to the broad-line region in this galaxy.

Except for the presence of the broad base in Brγ, our results are in good agreement with those of Veilleux et al. (1997), which also found that Paβ and H_2 $v = 1-0$ S(1) were narrower than [Fe II] 1.26 μm or Brγ, with this last line presenting an intrinsic width of $\sim$550 km s^{-1}. Taking the narrow component of Brγ as containing about one-third of the observed line flux, the H_2/Brγ ratio is $\sim$1.2, and would indicate some marginal evidence of H_2 excitation by X-rays from the active nucleus. Using the same assumptions as for IC 5063, the observed luminosity of H_2 $v = 1-0$ S(1) in the inner 3 arcsec translates into a mass of hot H_2 of $\approx$300 $M_\odot$.

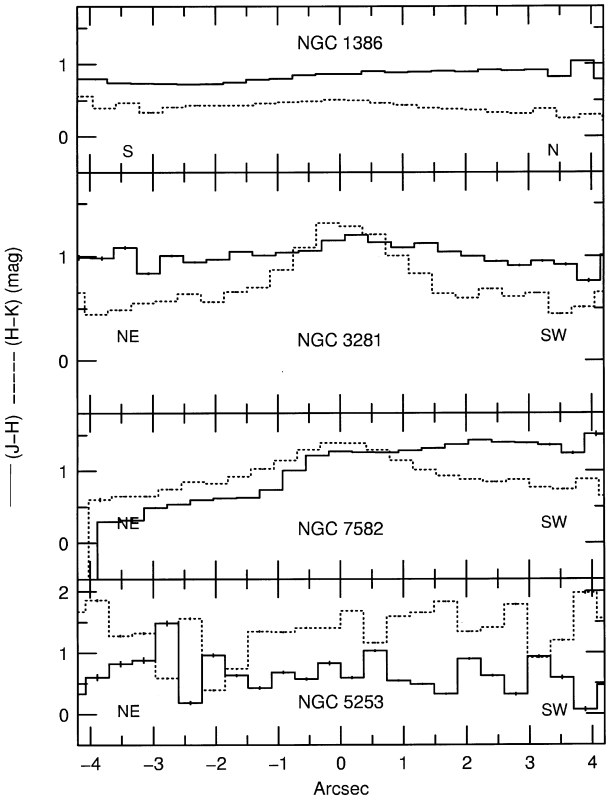

Figure 20. Four representative ($J-H$) (full line) and ($H-K$) (dotted line) colour profiles derived from the XD spectra of the sample galaxies. The orientation is the same as for the line profiles shown in Section 3.1, and is also indicated in the individual panels.

3.2 Continuum

In this section, we present and analyse ($J-H$) and ($H-K$) colour profiles derived from our XD spectra. Previous studies of the central (less than 1 kpc) regions of Seyfert galaxies have shown that their near-IR colours are well explained either by a mixture of an evolved stellar population plus emission from hot (800–1200 K) dust, with varying foreground reddening (Alonso-Herrero, Ward & Kotilainen 1996, hereafter AH96), or by a model more closely associated with the dusty torus scenario, in which the starlight is not significantly reddened, while the nuclear continuum source is represented by hot dust ($T \approx 1200$ K) reddened by $A_V \approx$ 5–30 mag (Alonso-Herrero et al. 1998, hereafter AH98). The off-nuclear colours show little evidence of hot dust emission, except for a few cases where the effect is attributed to the presence of massive stars acting as heating sources.

To obtain the colour profiles, the calibrated spectra were rebinned to 0.8 arcsec pixel^{-1}, then multiplied by the transmission

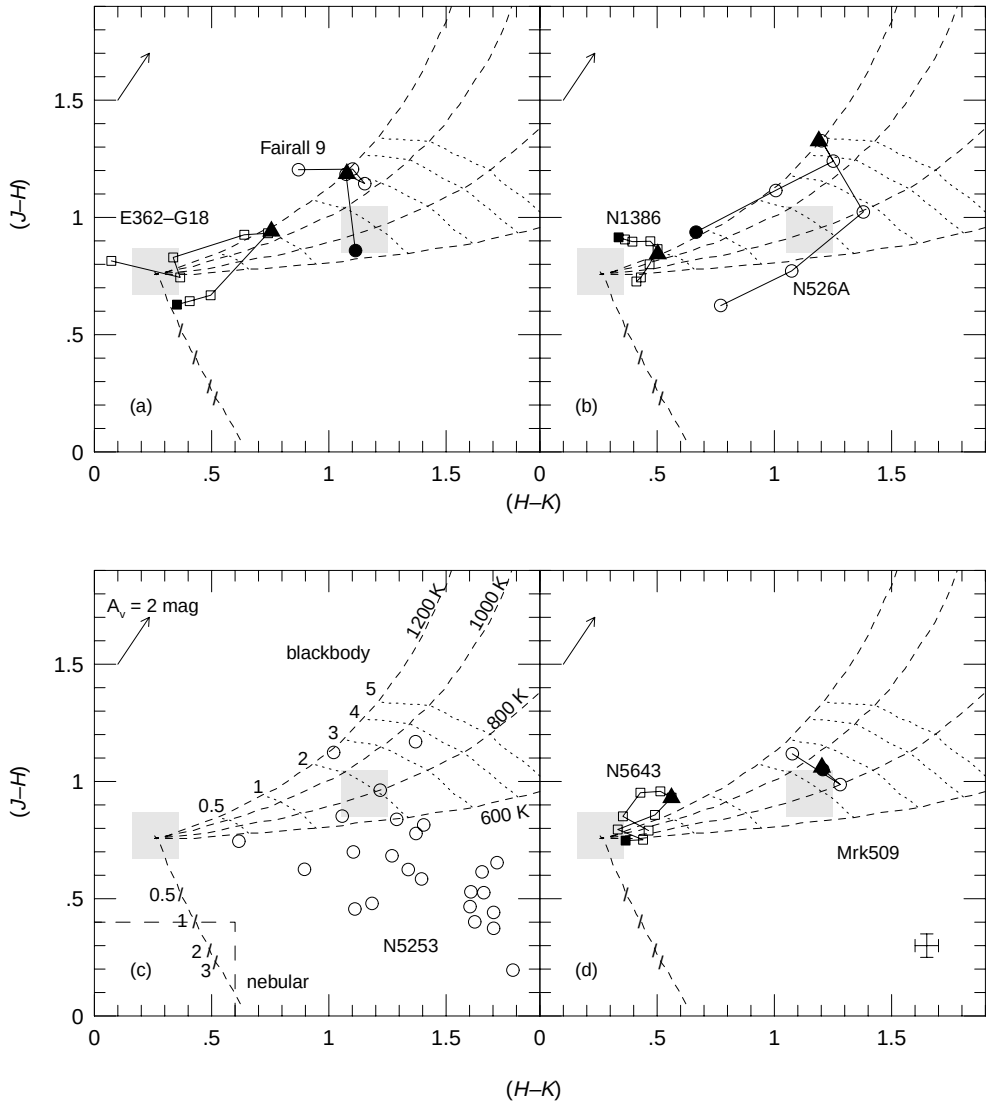

Figure 21. $(J - H)$ versus $(H - K)$ colour–colour diagrams (adapted from AH98). See text for an explanation of the mixing curves and other symbols. For each object, the filled triangle represents the nucleus, while the filled circle/square is the most distant point from the nucleus on the cone (positive) side of the profile. The bin size is 0.8 arcsec and the spatial interval (in arcsec) represented is as follows: (a) ESO 362-G18 (−3.4 NE, 3 SW) and Fairall 9 (−2.6 SE, 1.4 NW); (b) NGC 1386 (−3.4 S, 3 N) and NGC 526A (−2.6 NW, 3 SE); (c) NGC 5253 (−4 NE, 4 SW; bin 0.4 arcsec); (d) NGC 5643 (−3.4 W, 3.8 E) and Mrk 509 (−1.8 N, 1.4 S). (e) NGC 5728 (circles) PA = 20° (−3.4 NE, 3.8 SW), (squares) PA = 110° (−3.4 NW, 3.8 SE) and NGC 4388 (circles) PA = 13° (−3.4 NE, 2 SW), (squares) PA = 90° (−3.4 W, 3.8 E); (f) NGC 1365 (−2.8 NW, 3.8 SE); (g) NGC 3281 (−3.4 NE, 3 SW); (h) NGC 2110 (−3.4 SE, 3.8 NW) and NGC 7582 (−3.4 NE, 3.8 SW).

Table 6. Nuclear and bulge colours.

Object	Nucleus ($R < 0.8$ arcsec)			Bulge ($0.8 < R < 2$ arcsec)				
	$(J - H)$	$(H - K)$		$(J - H)$	$(H - K)$		$(J - H)$	$(H - K)$
NGC 526A	1.27 ± 0.03	1.24 ± 0.04	NW	0.88 ± 0.07	1.25 ± 0.10	SE	1.12 ± 0.03	0.99 ± 0.13
NGC 1365	1.07 ± 0.03	0.97 ± 0.03	NW	0.78 ± 0.03	0.94 ± 0.08	SE	1.05 ± 0.03	0.57 ± 0.05
NGC 1386	0.87 ± 0.01	0.49 ± 0.01	S	0.77 ± 0.02	0.45 ± 0.01	N	0.89 ± 0.01	0.40 ± 0.02
NGC 2110	1.01 ± 0.01	0.94 ± 0.02	SE	1.02 ± 0.02	0.66 ± 0.07	NW	1.01 ± 0.04	0.68 ± 0.05
NGC 3281	1.13 ± 0.03	1.21 ± 0.06	NE	1.02 ± 0.01	0.72 ± 0.06	SW	1.08 ± 0.02	0.79 ± 0.10
NGC 4388 (13)	0.89 ± 0.01	1.42 ± 0.03	N	0.88 ± 0.02	1.19 ± 0.04	S	1.02 ± 0.07	1.16 ± 0.04
NGC4388 (90)	1.03 ± 0.02	1.51 ± 0.02	W	0.85 ± 0.05	1.35 ± 0.04	E	1.01 ± 0.01	1.28 ± 0.08
NGC 5643	0.93 ± 0.01	0.54 ± 0.01	W	0.94 ± 0.02	0.41 ± 0.03	E	0.82 ± 0.02	0.42 ± 0.05
NGC 5728 (110)	0.94 ± 0.02	0.45 ± 0.03	NW	0.84 ± 0.01	0.53 ± 0.02	SE	0.94 ± 0.01	0.32 ± 0.01
NGC 5728 (20)	1.04 ± 0.03	0.39 ± 0.03	NE	0.87 ± 0.05	0.51 ± 0.01	SW	1.12 ± 0.01	0.11 ± 0.05
NGC 7582	1.21 ± 0.04	1.33 ± 0.03	NE	0.70 ± 0.06	0.99 ± 0.07	SW	1.31 ± 0.03	1.02 ± 0.06
ESO 362-G18	0.90 ± 0.04	0.69 ± 0.04	NE	0.84 ± 0.03	0.38 ± 0.05	SW	0.65 ± 0.01	0.44 ± 0.03
Fairall 9	1.14 ± 0.03	1.11 ± 0.02	SE	1.19 ± 0.02	1.08 ± 0.07	NW	0.77 ± 0.05	1.06 ± 0.03
Mrk 509	0.98 ± 0.05	1.24 ± 0.02	N	1.11 ± 0.07	1.05 ± 0.13	S	0.59 ± 0.06	1.07 ± 0.07

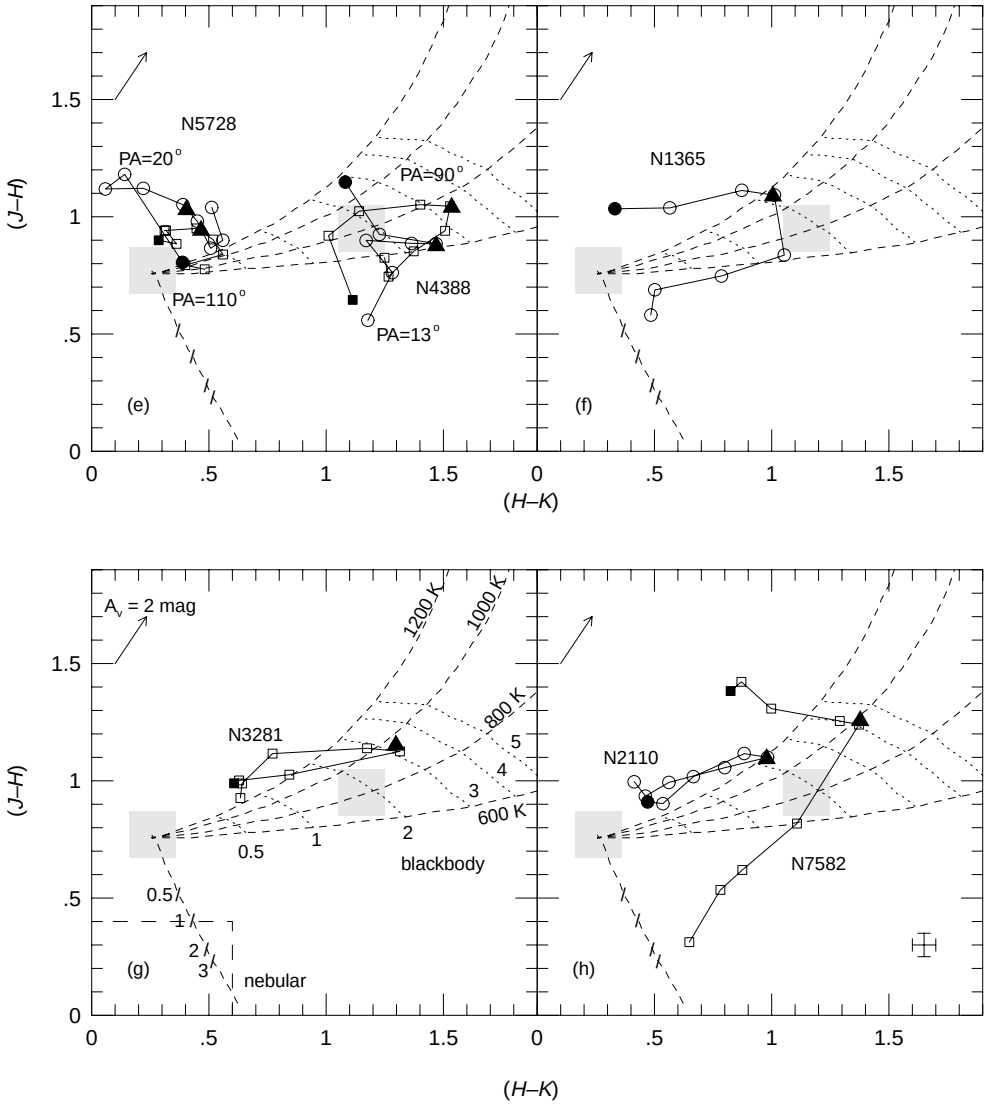

Figure 21 – *continued*

curve of the corresponding filter, obtained from the CTIO web site,[2] integrated along the wavelength direction and converted from flux to magnitudes. With an average seeing of 1–1.5 arcsec, each profile is sampled by 1–2 pixels.

Table 6 lists the nuclear ($r < 0.8$ arcsec) and 'bulge' ($0.8 < r < 2$ arcsec) colours derived from the above profiles. These intervals correspond to linear scales of ~45 to 750 pc for the inner and outer radii in the Seyfert 2 galaxies in the sample. The errors correspond to the rms around the mean of the colour in the aperture, not the observational error. Fig. 20 shows four representative colour profiles: some are very flat, as in NGC 1386, while others show redder $(H - K)$ colour in the nuclear region or asymmetric profiles, as in NGC 3281 and 7582, respectively. The colours in NGC 5253 are highly inhomogeneous, as might be expected from the clumpy nature of the distribution of the gas and presumably the reddening in this galaxy.

The data in Table 6 are in agreement with previous conclusions (AH96; AH98; Kotilainen et al. 1992, hereafter K92) that the nuclei of Seyferts tend to be redder than their bulges in one or both $(J - H)$, $(H - K)$ colours. Using the full profile, our data agree with the 1.5 and 3-arcsec aperture photometry colours published in the literature within 0.1–0.2 mag for most objects, except NGC 4388, where our $(H - K)$ colour is ~0.5 mag redder than the published values (AH96; AH98). We also find that for a few galaxies there is a 0.3–0.4 mag difference in the colours, most remarkably $(J - H)$, of the 'bulge' regions at opposite sides of the nucleus.

The $(J - H)$ versus $(H - K)$ colour–colour diagrams of Figs 21(a) to (f) are based on the work of AH98. The shaded square to the left represents the colours of bulges of normal spiral galaxies (a late-type stellar population), while the one to the right represents the typical colours of quasars, corrected to zero redshift. The area bounded by dashed lines in the lower left corner of Figs 21(c) and (g) corresponds to the region occupied by a young/intermediate-age stellar population component with ages ranging from 10^6 to 10^8 yr, calculated from the models of Leitherer & Heckman (1995). The arrow in the upper left-hand corner represents the effects of 2 mag of visual extinction. The 'mixing curves' represented by the dashed lines are the colours of

[2] We have used the curves of the filters in use with the CIRIM camera: j40, h44 and k50, for *J*, *H* and *K*, respectively.

the sum of a late-type stellar population and either a blackbody component (assumed to be representative of hot dust emission) with temperatures $T = 600$, 800, 1000 and 1200 K, or a nebular component, corresponding to hydrogen and helium continuum and line emission. The dotted lines (diagonal slashes) are the loci of the colours for the given ratio of dust (nebular) and stellar luminosities in the K band. The results for each individual galaxy are described below.

NGC 5253. Fig. 21(c) – the data points are scattered over the bottom right of the diagram. Since the long-slit spectrum indicates little or no continuum emission, the data can be understood as nebular emission plus spatially inhomogeneous reddening and/or dust emission. From the Brγ/Paβ ratio, we found regions with $A_V \sim 8$ mag, which would be enough to shift the points from the nebular emission curve to the observed location at the middle of the diagram.

NGC 526A. Fig. 21(b) – the data points follow different paths in the cone (south-east) and anti-cone (north-west) directions, with the $(J - H)$ colour in the region 0.8–1.4 arcsec south-east about 0.3 mag redder than to the north-west. This behaviour suggests a difference in the underlying stellar population content between the two sides of the nucleus. As can be seen in Fig. 21, the loci of old (left grey square) and young–intermediate (area at bottom left limited by dashed lines) stellar populations are separated by $\sim$0.8 mag in $(J - H)$, with very little difference in the corresponding $(H - K)$ colours. Reddening effects are also very likely to be present and cannot be discarded as contributing to the observed colours. In the central bin (0.8 arcsec), the colours suggest that hot dust emission dominates the continuum.

NGC 1365. Fig. 21(f) – the colours behave somewhat similarly to NGC 526A, although with the nuclear colour corresponding to a smaller ratio of hot dust to starlight emission. The bluer $(J - H)$ colour towards the north-west may result from contamination of the 'normal', old bulge population by younger stars in the 'hotspots' (see Storchi-Bergmann & Bonatto 1991; Morganti et al. 1999).

NGC 1386. Fig. 21(b) – both colour profiles (Fig. 20) are essentially flat, with $(J - H)$ rising slightly towards the north (the optical cone direction) and $(H - K)$ showing only a hint of a redder colour in the nuclear region. In the colour–colour plot, the points concentrate near the pure bulge region, with little or no contribution from hot dust. The orientation of both the high-excitation optical and radio emission (Weaver et al. 1991; Storchi-Bergmann et al. 1996), as well as the fact that NGC 1386 contains water vapour megamaser emission (Braatz, Wilson & Henkel 1996), suggests that the collimating structure is seen edge-on. Therefore the hot dust in the inner regions may be obscured by colder dust further out in the disc, resulting in a small contribution from the nucleus to the near-infrared continuum.

NGC 2110. Fig. 21(h) – the analysis of the J- and K-band continua presented in Paper I indicates the presence of a hot dust component in the inner $\sim$150 pc, consistent with emission by a circumnuclear torus. The observed colour profiles confirm this finding: while the $(J - H)$ distribution is essentially flat across the nucleus, the $(H - K)$ colour increases by about 0.5 mag in the inner 2 arcsec relative to the external regions. In the colour–colour diagram, ignoring the foreground galactic reddening [$E(B - V)_G \sim 0.36$: Burstein & Heiles 1982], the points trace a continuous path from pure bulge colours to a combination of bulge and a $\sim$1200-K blackbody component at the nucleus.

NGC 3281. Fig. 21(g) – the colour profiles (Fig. 20) present a similar behaviour to that observed in NGC 2110, with the variation in $(H - K)$ colour being even more pronounced, with a 0.7-mag decrease from the nucleus to the bulge. This would indicate a higher fraction of hot dust emission in the nuclear region than in the NGC 2110 case, but of a somewhat lower temperature ($\sim$1000 K).

NGC 4388. Fig. 21e – the $(H - K)$ colour is redder at the nucleus than in the bulge at PA=13°, similar to what is observed in NGC 2110 and 3281. The effect is much less apparent at PA = 90°, which can be understood if, as mentioned in Section 3.1, we missed the nucleus on this observation. Both PAs occupy the same region in the colour diagram, and the data points for the whole inner 5–6 arcsec ($\sim$1 kpc) are shifted towards redder $(H - K)$ colours when compared with other published values (K92; AH98).

NGC 5643. Fig. 21(d) – the colour profiles are flat across the nucleus. In the colour diagram, the points cluster near the bulge colours, with a small contribution from dust emission or a foreground reddening of $A_V \sim 1.5$–2 mag. Again, this could be a case of a torus either too cold to emit in the near-infrared or with inner regions obscured from our line of sight by the outer ones.

NGC 5728. Fig. 21(e) – for PA = 110°, both colour profiles are rather flat. In the colour–colour plot, the data points cluster close to normal bulge colours, similar to what is observed for NGC 5643. Along the perpendicular direction (PA = 20°), $(J - H)$ is somewhat redder and $(H - K)$ bluer towards the south-west than to the north-east.

NGC 7582. Fig. 21(h) – the $(H - K)$ profile (Fig. 20) exhibits the same behaviour as observed in NGC 2110 and 3281, with the nuclear colour $\sim$0.5 mag redder than the bulge. The $(J - H)$ profile, however, rises steadily to the south-west, with a 0.8-mag increase from 3 arcsec north-east to 3 arcsec south-west (the cone side). In the colour–colour diagram, the nucleus corresponds to a dominant contribution from $\sim$1000-K blackbody emission. The data points starting at 3 arcsec north-east can be interpreted as a reddened evolving starburst, with increasing reddening towards the nucleus (up to $A_V \sim 8$ mag). The colours observed on the south-west (cone) side of the nucleus are suggestive of a reddened, old stellar population.

ESO 362-G18. Fig. 21(a) – the data points start with bulge colours at 3 arcsec north-east, run along a line of increasing contribution from hot dust, up to a maximum of equal contributions from both sources at the nucleus, and then return with $(J - H)$ colours $\sim$0.2 mag bluer towards the south-west. This effect can again be explained by a different underlying stellar population: an evolving starburst is bluer in $(J - H)$ but occupies almost the same region in $(H - K)$ as the typical late-type, bulge population.

Mrk 509 and *Fairall 9.* Figs 21(d) and (a) – the PSF of the nucleus dominates the inner 4 arcsec owing to the brightness of the central source. Since the sources are unresolved, the data points cluster around the colours characteristic of quasars, as expected for these type 1 Seyfert galaxies.

4 SUMMARY AND CONCLUSIONS

We have obtained near-infrared, long-slit spectra for a sample of 12 Seyfert 2s, 3 Seyfert 1s, and the starburst galaxy NGC 5253, using as the main selection criterion the presence of extended high-excitation emission observed in optical images. From our analysis of the spatial and spectral emission-line profiles, and of the continuum $(J - H)$ and $(H - K)$ colours, we conclude the following.

(i) Consistent with the selection criteria, nine of the 12 objects with extended optical emission lines also present extended emission lines in the near-IR along the position angle of the optical ionization cones or radio emission. In three cases, however, we found that the near-IR emission lines were also extended along PAs oriented perpendicular to the optical/radio emission axis. The clearest case where high-excitation near-IR line emission traces the optical ionization structure is NGC 7582, where the emission lines in the inner few arcsec are extended along the direction of the optical cone. Interestingly, the maxima of the emission-line distributions in this galaxy are consistently offset from the peak of the continuum emission by ~0.8 arcsec in the direction opposite to the optical cone. Besides the central peak, the spatial profile of the [Fe II] 1.64-μm line in NGC 7582 presents a secondary structure between 0.5 and 2.5 arcsec south-west, with the [Fe II] 1.64 μm/Paβ ratio increasing from ≈0.5 at the position of the continuum peak to 4.4 at 1.6 arcsec south-west, indicating a different ionization mechanism for the [Fe II] line in this region. A similar result was found for NGC 1386, for which the [Fe II] 1.26 μm/Paβ ratio rises from ≈2 to 6 between the nucleus and the optical extended emission-line region at 2 arcsec north. These high values and the presence of radio emission and/or a high-velocity nuclear outflow spatially coincident with the optical extended narrow-line region suggest that shocks may play a role as an excitation mechanism for the off-nuclear [Fe II] line in both galaxies.

(ii) The low-resolution (XD) spectra are not sufficiently sensitive to detect the expected H_2 emission from the torus. However, in the few cases for which we have a high-resolution *K*-band spectrum (Mrk 573, IC 5063, NGC 2110), the H_2 S(1) λ 2.12 μm was clearly detected.

(iii) Broad components have been observed in the permitted emission lines of the Seyfert 1 galaxies, in nuclear Paβ in NGC 1365, and very likely in Brγ in Mrk 573. In NGC 1365 the flux of the broad (FWHM ≈ 1500 km s^{-1}) component of Paβ was used to estimate a reddening of $A_V \sim 8$ mag towards the broad-line region. A lower limit of ~9 mag was obtained for A_V towards the broad-line region of Mrk 573. In NGC 4388 and Mrk 573 the [S IX] λ 1.262-μm emission line was detected, and found to be spatially unresolved in both objects. With an ionization potential of 0.328 keV, the detection of this species is indirect evidence of significant soft X-ray continuum flux in these galaxies. In NGC 5253, the Brγ/Paβ ratio was used to map strong reddening variations, from $A_V \sim 0$ to 6 mag within the central 8 arcsec.

(iv) Spatial $(J-H)$ and $(H-K)$ colour profiles were derived from our spectra. For most Seyfert 2s, the nuclear colours are redder than the extranuclear values, with the nuclear continuum being dominated by hot ($T \sim 1000$ K) dust emission in NGC 1365, NGC 2110, NGC 3281, NGC 7582 and ESO 362-G18. In NGC 1386, 5643 and 5728, the nuclear colours are consistent with a continuum dominated by the emission from the underlying stellar population plus a smaller contribution from dust and/or foreground reddening effects. The Seyfert 1 nuclei, Mrk 509 and Fairall 9, have colours similar to quasars, as expected.

(v) The galaxies NGC 526A, NGC 1365, NGC 7582 and ESO 362-G18 show a clear difference between the $(J-H)$ colours on each side of the nucleus. Since late-type (bulge) and young/intermediate stellar populations differ mostly in their $(J-H)$ colour, $(H-K)$ being approximately the same, we explain this effect by differences in the underlying stellar population, very likely coupled with reddening. The observed colour differences could indicate the presence of a younger/intermediate-age component, associated, for example, with the star-forming rings known to exist in some of the observed galaxies, and which could provide a larger contribution to the near-IR continuum on one side of the nucleus relative to the other.

ACKNOWLEDGMENTS

This work has made use of NASA's Astrophysics Data System Abstract Service (ADS), and of the NASA/IPAC Extragalactic Database (NED) which is operated by the Jet Propulsion Laboratory, California Institute of Technology, under contract with the National Aeronautics and Space Administration. Research was partially supported by the Brazilian Agencies FAPERGS and CNPq. The Cerro Tololo Interamerican Observatory is operated by the Association of Universities for Research in Astronomy, Inc., under contract with the National Science Foundation. IRAF is distributed by the National Optical Astronomy Observatories, which are operated by the Association of Universities for Research in Astronomy, Inc., under cooperative agreement with the National Science Foundation.

REFERENCES

Alonso-Herrero A., Ward M. J., Kotilainen J. K., 1996, MNRAS, 278, 902 (AH96)
Alonso-Herrero A., Rieke M. J., Rieke G. H., Ruiz M., 1997, ApJ, 482, 747
Alonso-Herrero A., Simpson C., Ward M. J., Wilson A. S., 1998, ApJ, 495, 196 (AH98)
Antonucci R. R. J., 1993, ARA&A, 31, 473
Blietz M., Cameron M., Drapatz S., Genzel R., Krabbe A., van der Werf P., Sternberg A., Ward M., 1994, ApJ, 421, 92
Braatz J. A., Wilson A. S., Henkel C., 1996, ApJS, 106, 51
Burstein D., Heiles C., 1982, AJ, 87, 1165
Calzetti D., Meurer G. R., Bohlin R. C., Garnett D. R., Kinney A. L., Leitherer C., Storchi-Bergmann T., 1997, AJ, 114, 1834
Colina L., 1993, ApJ, 411, 565
Falcke H., Wilson A. S., Simpson C., 1998, ApJ, 502, 199
Fischer J., Smith H. A., Geballe T. R., Simon M., Storey J. W. V., 1987, ApJ, 320, 667
Forbes D. A., Ward M. J., 1993, ApJ, 416, 150
Giannuzzo E. M., Stirpe G. M., 1996, A&A, 314, 419
Glass I. S., Moorwood A. F. M., 1985, MNRAS, 214, 429
Kawara K., Nishida M., Gregory B., 1990, ApJ, 352, 433
Kotilainen J. K., Ward M. J., Boisson C., DePoy D. L., Bryant L. R., Smith M. G., 1992, MNRAS, 256, 149 (K92)
Kristen H., Jörsäter S., Lindblad P. O., Boksenberg A., 1997, A&A, 328, 483
Krolik J. H., Begelman M. C., 1988, ApJ, 329, 702
Kulkarni V. P. et al., 1998, ApJ, 492, L121
Leitherer C., Heckman T. M., 1995, ApJS, 96, 9
Lumsdey S. L., Puxley P. J., 1996, MNRAS, 281, 493
Marco O., Alloin D., Beuzit J. L., 1997, A&A, 320, 399
Miller J. S., Goodrich R. W., 1990, ApJ, 378, 47
Moorwood A. F. M., Oliva E., 1990, A&A, 239, 78
Moorwood A. F. M., van der Werf P. P., Kotilainen J. K., Marconi A., Oliva E., 1996, A&A, 308, 1
Morganti R., Oosterloo T., Tsvetanov Z., 1998, AJ, 115, 915
Morganti R., Tsvetanov Z. I., Gallimore J., Allen M. G., 1999, A&AS, 137, 457
Mulchaey J. S., Wilson A. S., Tsvetanov Z. I., 1996, ApJS, 102, 309
Nagar N. M., Wilson A. S., Mulchaey J. S., Gallimore J., 1999, ApJS, 120, 209

Osterbrock D. E., 1989, Astrophysics of Gaseous Nebulae and Active Galactic Nuclei. University Science Books, Mill Valley, CA
Phillips M. M., Baldwin J. A., Atwood B., Carswell R. F., 1983, ApJ, 274, 558
Pier E. A., Krolik J. H., 1993, ApJ, 418, 673
Pogge R. W., 1989, ApJ, 345, 730
Pogge R. W., de Robertis M. M., 1995, ApJ, 451, 585
Schmitt H. R., Storchi-Bergmann T., Baldwin J. A., 1994, ApJ, 423, 237
Schmitt H. R., Storchi-Bergmann T., Cid Fernandes R., 1999, MNRAS, 303, 173
Scoville N. Z., Hall D. N. B., Ridgway S. T., Kleinmann S. G., 1982, ApJ, 253, 136
Simpson C., Ward M., Kotilainen J., 1994, MNRAS, 271, 250
Simpson C., Forbes D. A., Baker A. C., Ward M. J., 1996a, MNRAS, 283, 777
Simpson C., Mulchaey J. S., Wilson A. S., Ward M. J., Alonso-Herrero A., 1996b, ApJ, 457, L19
Simpson C., Wilson A. S., Bower G., Heckman T. M., Krolik J. H., Miley G. K., 1997, ApJ, 474, 121
Stevens I. R., Forbes D. A., Norris R. P., 1999, MNRAS, 306, 479
Stone J. L., Jr, Wilson A. S., Ward M. J., 1988, ApJ, 330, 105
Storchi-Bergmann T., Bonatto C. J., 1991, MNRAS, 250, 138
Storchi-Bergmann T., Baldwin J. A., Wilson A. S., 1993, ApJ, 410, L11
Storchi-Bergmann T., Rodriguez-Ardila A., Schmitt H. R., Wilson A. S., Baldwin J. A., 1996, ApJ, 472, 83
Storchi-Bergmann T., Winge C., Ward M. J., Wilson A. S., 1999, MNRAS, 304, 35 (Paper I)
Tran H. D., 1995, ApJ, 440, 597
Vanzi L., Alonso-Herrero A., Rieke G. H., 1998, ApJ, 504, 93
Veilleux S., Goodrich R. W., Hill G. J., 1997, ApJ, 477, 631
Veilleux S., Bland-Hawthorn J., Cecil G., Tully R. B., Miller S. T., 1999, ApJ, 520, 111
Véron P., Lindblad P. O., Zuiderwijk E. J., Adam G., Véron M. P., 1980, A&A, 87, 245
Weaver K. A., Wilson A. S., Baldwin J. A., 1991, ApJ, 366, 50
Wilson A. S., Tsvetanov Z. I., 1994, AJ, 107, 1227
Wilson A. S., Baldwin J. A., Ulvestad J. S., 1985, ApJ, 291, 627
Wilson A. S., Braatz J. A., Heckman T. M., Krolik J. H., Miley G. K., 1993, ApJ, 419, L61

This paper has been typeset from a TEX/LATEX file prepared by the author.